



RESEARCH ARTICLE

10.1029/2022GC010619

Key Points:

- A generalized strategy (GC_SRF) for obtaining the lithospheric thickness from S-wave receiver functions is proposed
- This GC_SRF strategy can rebuild the Sp converted phase from either full wavefield synthetic seismograms or field data without artifacts
- Distinct lateral variations in the lithospheric thickness from the Sichuan Basin to Tengchong Volcano in southeastern Tibet are revealed

Supporting Information:

Supporting Information may be found in the online version of this article.

Correspondence to:

Y. Deng,
yangfandeng@gig.ac.cn

Citation:

Zhang, Z., & Deng, Y. (2022). A generalized strategy from S-wave receiver functions reveals distinct lateral variations of lithospheric thickness in southeastern Tibet. *Geochemistry, Geophysics, Geosystems*, 23, e2022GC010619. <https://doi.org/10.1029/2022GC010619>

Received 19 JUL 2022
Accepted 28 OCT 2022



Author Contributions:

Conceptualization: Yangfan Deng
Data curation: Zhou Zhang
Funding acquisition: Yangfan Deng
Methodology: Zhou Zhang, Yangfan Deng
Project Administration: Yangfan Deng
Visualization: Zhou Zhang
Writing – original draft: Zhou Zhang
Writing – review & editing: Yangfan Deng

© 2022. The Authors.

This is an open access article under the terms of the [Creative Commons Attribution-NonCommercial-NoDerivs License](https://creativecommons.org/licenses/by/4.0/), which permits use and distribution in any medium, provided the original work is properly cited, the use is non-commercial and no modifications or adaptations are made.

A Generalized Strategy From S-Wave Receiver Functions Reveals Distinct Lateral Variations of Lithospheric Thickness in Southeastern Tibet

Zhou Zhang^{1,2,3}  and Yangfan Deng^{1,2} 

¹State Key Laboratory of Isotope Geochemistry, Guangzhou Institute of Geochemistry, Chinese Academy of Sciences, Guangzhou, China, ²CAS Center for Excellence in Deep Earth Science, Guangzhou, China, ³College of Earth and Planetary Sciences, University of Chinese Academy of Sciences, Beijing, China

Abstract The selected rotation angle and deconvolution time window during S-wave receiver function (SRF) calculations, and the final SRF quality control may introduce artificial interference. Here we overcome these problems by proposing a new strategy named GC_SRF for obtaining the lithospheric thickness from S-wave receiver functions, which employs grid search and correlation analysis to obtain reliable SRFs. Extensive tests using synthetic and real data suggest that the GC_SRF strategy is a robust and reproducible approach for estimating lithospheric thickness. Specifically, this GC_SRF strategy can restore the weak Sp phases from full wavefield synthetic seismograms. Clear and distinct discontinuity patterns that do not involve artificial interference compared with those obtained in previous studies of southeastern Tibet are produced here. The post-stack migrated SRFs reveal distinct lateral variations of lithospheric thickness in southeastern Tibet: (a) Tengchong volcano has a thin crust and thin lithosphere–asthenosphere boundary (LAB) (~90 km); (b) the Chuandian region has a thicker crust and either a poorly defined or unclear LAB. The absence of a continuous LAB in the Chuandian region may suggest lithospheric regrowth due to the recovery processes of the mantle plume; (c) a thinner crust and clear LAB of ~160 km depth is presented beneath the Sichuan Basin.

Plain Language Summary The outermost shell of the solid Earth, the lithosphere, is the “Birthplace” of numerous natural hazards, such as volcanic eruptions or destructive earthquakes. The thickness and property of the lithosphere are crucial for understanding the evolutionary processes of the Earth, yet potential artificial interferences are difficult to avoid in conventional seismological techniques. In this study, we introduce a new strategy (GC_SRF) to obtain the lithospheric thickness while avoiding potential artificial interference based on the teleseismic technique. This newly developed strategy can obtain robust and reliable lithospheric thickness from synthetic seismograms. The GC_SRF is then applied to image the lithospheric structure beneath the southeastern Tibetan Plateau, where distinct lateral variations of lithospheric thickness are revealed. Further application of this strategy to other complex geological environments will help to advance the understanding of geodynamic processes.

1. Introduction

The lithosphere–asthenosphere boundary (LAB) is generally considered to be a negative velocity gradient (NVG) transition zone from the cold and fast lithosphere to the warm and slow asthenosphere. Its depth varies considerably, ranging from ~0 km in mid-oceanic ridge, to <50 km beneath the young oceans, and then to >200 km beneath cratonic regions (Bostock, 1999; Fischer et al., 2010, 2020; Hopper & Fischer, 2015; Thybo, 2006). The precise positioning of the LAB provides good constraints on the evolution of cratons and orogens, such as lithospheric thinning owing to extension (e.g., Buck, 1991) or detachment (e.g., Davies & Von Blanckenburg, 1995; Kosarev et al., 1999) and lithospheric thickening owing to collision (e.g., Houseman et al., 1981). A series of methods, such as receiver functions (P- and S-wave receiver function; PRF and SRF, respectively), SS precursors, and body-wave and surface-wave tomography, have been developed to detect the lithospheric thickness at both global (Bijwaard & Spakman, 2000; Ritsema et al., 2004; Ritzwoller et al., 2002) and local scales (Long et al., 2021; Mojaver et al., 2021; Rawlinson & Fishwick, 2012; Zhang et al., 2021).

SRF is the most widely used method for detecting the LAB because the Sp converted phase is remarkably sensitive to the vertical velocity gradient at the typical LAB depth. More importantly, even if the PRF has higher temporal and depth resolution in most cases, it has serious contamination by other phases across the

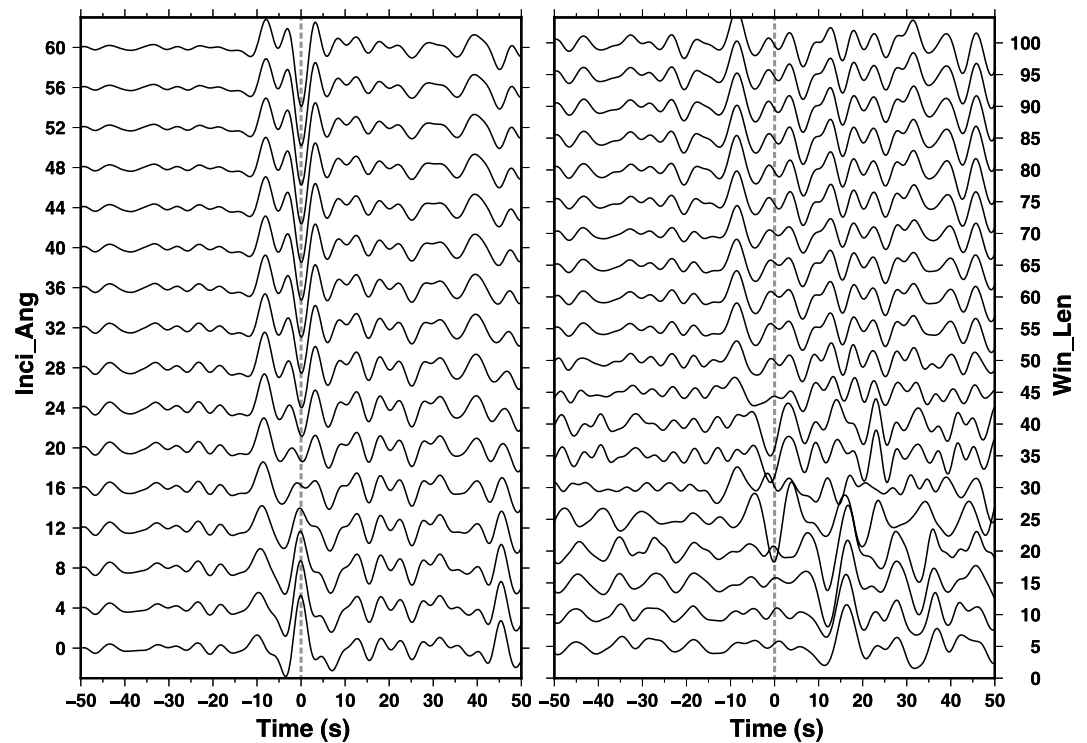


Figure 1. The influence of the incidence angle (Inci_Ang) and deconvolution time window length (Win_Len) on the shape of the S wave receiver function.

LAB depth (Chen et al., 2009; Hansen et al., 2010; Hu et al., 2011; Levander & Miller, 2012; Liu, Klemperer, & Blanchette, 2021; Liu & Zhao, 2021; Thybo et al., 2021; Zhang et al., 2014). Coordinate system rotation and deconvolution are important steps for obtaining SRFs. However, the incidence angle of the planar S wave could be affected by the near-surface structures beneath the seismic stations, and the estimated rotation angle based on the polarization of the S wave may be different from the synthetic value due to the complexity of the earthquake mechanism and the source time function (Chu et al., 2009; Fichtner et al., 2009; Tape et al., 2007; Vallée et al., 2011; Yuan et al., 2006). The deconvolution time window may also include mixtures of different seismic phases. Here, we identified the incidence angle (Inci_Ang) and the length of the source wavelet window (Win_Len) as the two key parameters in this study. We calculated the SRFs by varying these two parameters to mimic the three-component waveforms at station ST09 on the Tibetan Plateau, which has been analyzed in a previous study (Kumar et al., 2006). Figure 1 shows that different values of these two parameters can indeed affect the shape of the SRFs. The waveform amplitude at time zero could be either negative or positive for different Inci_Ang and Win_Len values. Furthermore, the quality control process of the estimated SRFs could also influence the stacking and migration results. Therefore, the inappropriate selection of the coordinate rotation angle and deconvolution time window, and following the quality control process would potentially bias the resultant LAB depth.

Various efforts have been made to optimize the coordinate rotation angle and quality control process to improve the reliability and stability of the constructed SRFs. Minimizing the amplitude at time zero (Kind et al., 2012; Kumar et al., 2006; Yuan et al., 2006; Zhang et al., 2012), measuring the polarization angle based on the S-wave particle motion (Farra & Vinnik, 2000; Vinnik et al., 2004), and converting from the apparent velocity (Hu et al., 2011; Reading et al., 2003) are all reliable approaches for determining the possible rotation angle. The quality control process includes visual inspection, signal-to-noise ratio (SNR) constraints (Hansen et al., 2010; Shen et al., 2019), and bootstrap estimation (Hansen et al., 2009; Xu et al., 2017, 2019). However, these methods could introduce artifacts based on the parameters chosen. A robust and reproducible strategy that avoids artificial interference when obtaining SRFs has not been implemented to date.

Here we focus on avoiding such artificial interference when obtaining the lithospheric thickness by varying *Inci_Ang* and *Win_Len* during the SRF calculation and then performing quality control on the resultant SRFs. We develop the generalized strategy (GC_SRF) for obtaining the lithospheric thickness from S-wave receiver functions to extract stable SRFs and guarantee reproducibility, where the “G” and “C” represent the grid search and correlation analysis, respectively. Specifically, we first perform a grid search to obtain the two parameters, *Inci_Ang* and *Win_Len*. We then analyze the SRFs corresponding to different combinations of these two parameters via cross-correlation to obtain the optimal SRF. The root mean square error (RMSE) algorithm is introduced to perform the quality control process in real data cases. Parallel computing is introduced to ensure the computational efficiency of the GC_SRF strategy. This strategy has been effectively applied to both full waveform synthetic seismograms and real data sets. Distinct lateral variations of lithospheric thickness are revealed in southeastern Tibet.

2. Method

The GC_SRF strategy is schematically illustrated in Figure 2. This approach contains coordinate rotation and discrete deconvolution (Farra & Vinnik, 2000; Wilson et al., 2006; Yuan et al., 2006) steps during the SRF calculation process. We follow the approach outlined in Kumar et al. (2006) and Yuan et al. (2006) to rotate the raw data from the ZNE system to the LQT system (L: aligned in the direction of P wave propagation; Q: aligned in the movement direction of SV phase; T: aligned in the movement direction of the SH phase) and determine the optimal *Inci_Ang* value by minimizing the amplitude at time zero on the *L* component.

The concept of discrete deconvolution has been employed in reflection seismology since the 1950s (Robinson & Treitel, 2000), and it was later introduced in passive seismology, where it has since been developed into different algorithms, such as time-domain iterative deconvolution (Ligorria & Ammon, 1999), wiener filter deconvolution (Wu et al., 2003a), water level deconvolution (Langston, 1979), maximum entropy spectrum deconvolution (Wu et al., 2003b), homomorphic deconvolution (Oppenheim, 1969; Ulrych et al., 1972), and spiking deconvolution (Robinson & Treitel, 1976, 2000; Treitel & Robinson, 1966). We have chosen spiking deconvolution in the GC_SRF strategy because of its wide use and efficiency in previous SRF studies (Farra & Vinnik, 2000; Kind et al., 2012; Yuan et al., 2006). Spiking deconvolution is employed in the LQT coordinate system to estimate an inverse filter based on a chosen time window of the Q-component waveform (Levinson, 1946; Rost & Thomas, 2002). The length of the time window (*Win_Len*) led directly to the instability of the deconvolution results (see Figure 1).

The spiking deconvolution algorithm that is used in most studies is enclosed in the Seismic Handler (Stammler, 1993), which is now inconvenient to use because it has not been maintained for nearly a decade. We therefore reconstruct the spiking deconvolution algorithm as a binary executable named *SX_Deconv* using the C++ compiler to handle and transplant the algorithm for different applications. We reproduce the results presented in Kumar et al. (2006) to validate the effectiveness of *SX_Deconv*. Figure 3 provides a comparison of the SRFs obtained by two algorithms for a Ms 6.4 earthquake event in 1998 at station ST09, with the Kumar et al. (2006) result shown in Figure 3a and the *SX_Deconv* result, where *Inci_Ang* varies from 0° to 60° and *Win_Len* is set to 85 s, as shown in Figure 3b. Specifically, there are identical SRFs on (a) and (b) that possess clear *Sp* phases, a positive *Smp* phase near −8 s, and a negative *SLp* phase near −18 s. Such a case can validate the application to obtain SRFs from both synthetic and real data.

The three-component waveforms recorded in the ZNE coordination system serve as the inputs for the GC_SRF strategy. We prepare the input data for the synthetic cases via the following procedure: (a) apply a 50- to 4-s bandpass filter; (b) clip the waveforms from 200 s before to 200 s after the theoretical S-wave arrival time, which is calculated using the IASP91 model (Kennett & Engdahl, 1991) and TauP Toolkit (Crotwell et al., 1999); and (c) detrend, demean, and resample the waveforms to 10 Hz. Similarly, the preparation steps for real data are almost the same as the synthetic cases, but in the first step we selected the teleseismic S waveforms for Ms ≥ 5.5 earthquakes that possess SNR_H greater than 5 with epicentral distances in the range of 50–90. Here we define the SNR_H as:

$$SNR_H = \frac{SNR_N + SNR_E}{2}, SNR = \left(\frac{1}{t_s} \sum S_i^2(t_s) \right) / \left(\frac{1}{t_n} \sum N_i^2(t_n) \right) \quad (1)$$

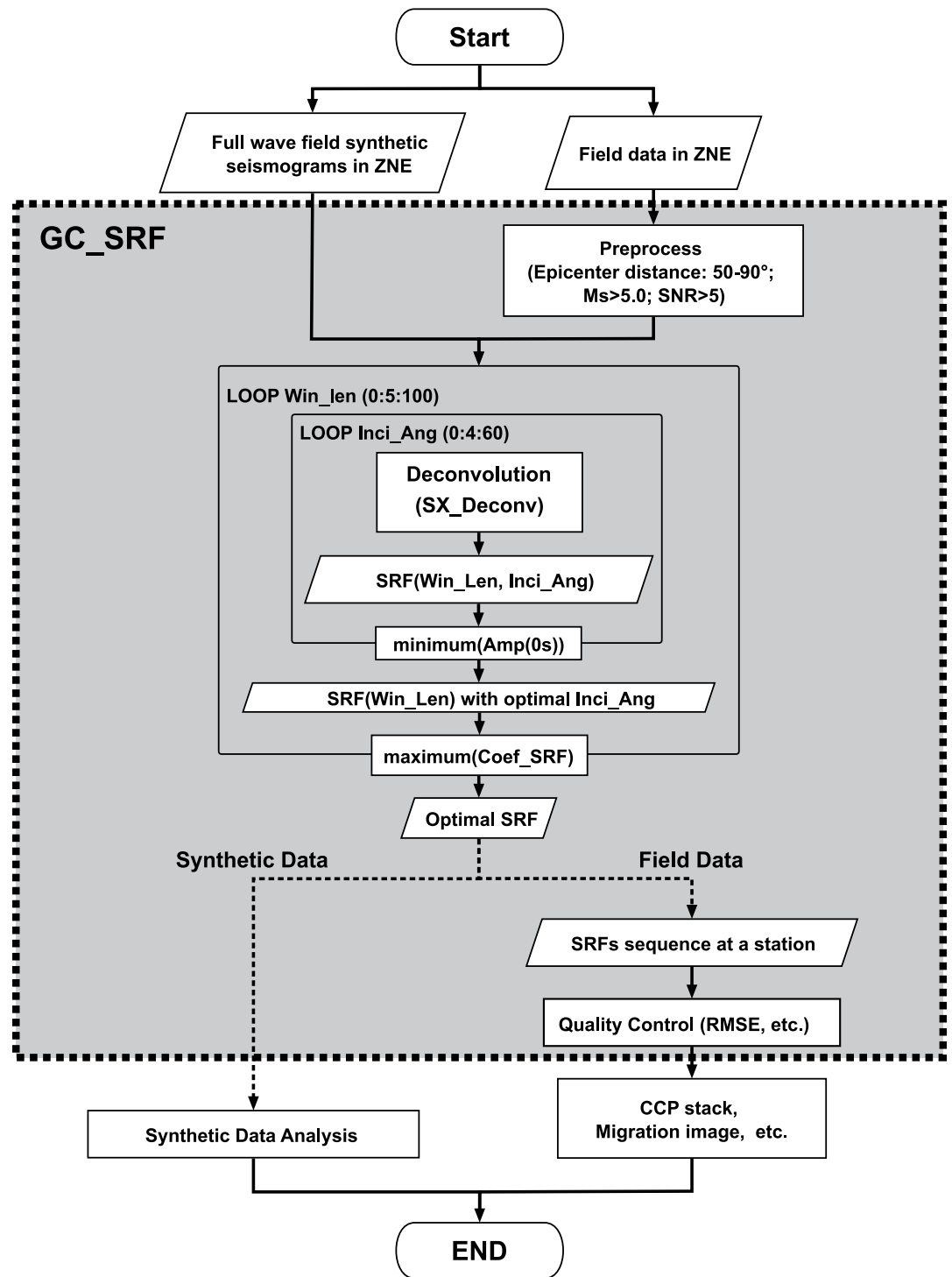


Figure 2. Flow chart of the GC_SRF strategy.

where SNR_N is the SNR of the N component and SNR_E is the SNR of the E component, with the signal window (t_s) defined as 5 s before to 30 s after the S-wave arrival time and the noise window (t_n) defined as 60 to 30 s before the S-wave arrival time.

The GC_SRF strategy calculates the SRFs corresponding to different $Inci_Ang$ and Win_Len values (i.e., $SRF(Inci_Ang, Win_Len)$). Here, $Inci_Ang$ is varied from 0° to 60° in 4° increments (Kumar et al., 2006), and

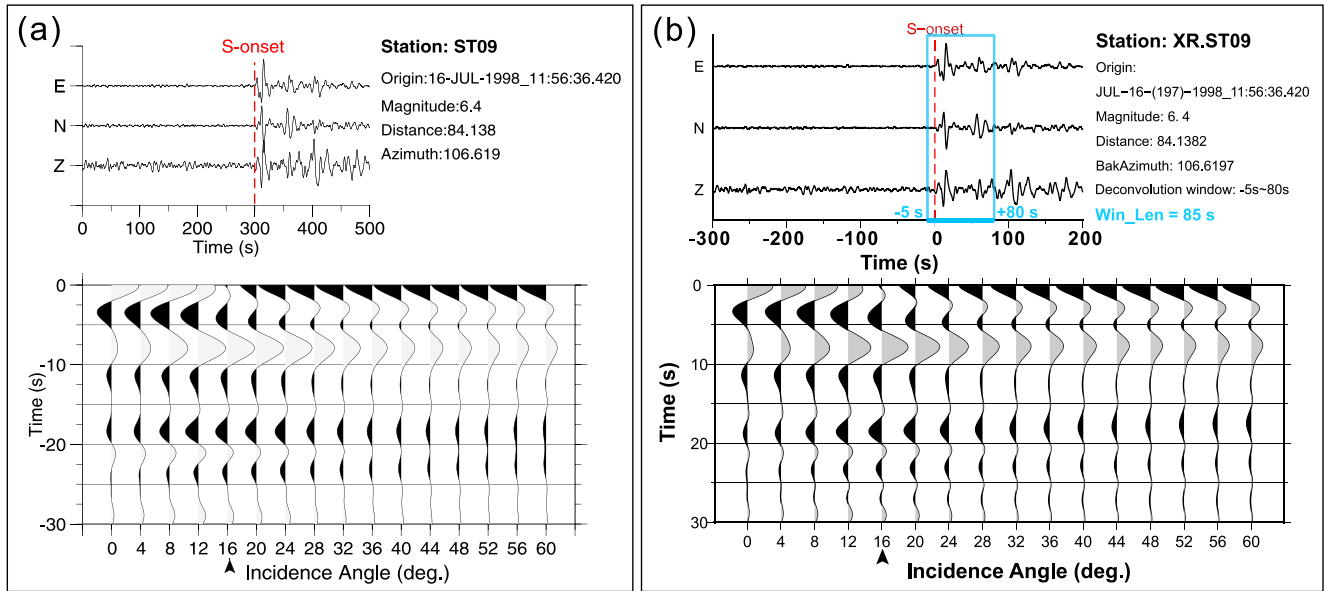


Figure 3. SRFs at station ST09 in southwestern Tibet with an Ms 6.4 earthquake event occurred in 1998. (a) An example edited from Figure 4b in Kumar et al. (2006). (b) Result from SX_Deconv. The top panel represents the original three-component event waveforms and event information. The bottom panel shows the SRFs corresponding to different incidence angles with deconvolution time window length fixed to 85 s. The upper panel in (a) and (b) show the raw teleseismic event waveform with earthquake information labeled, which indicates that the event waveform we collected from the Incorporated Research Institutions for Seismology (IRIS) is the same as that in Kumar et al. (2006). The lower panel in (a and b) are calculated SRFs for different rotation angles.

Win_Len is varied from 5 to 100 s in 5-s increments. There is only one SRF waveform for each Win_Len, with the smallest absolute amplitude occurring at time zero ($\text{SRF}_{\min(\text{Win_Len})}$). The arithmetic mean of these SRFs is redefined as the reference SRF (SRF_{ref}):

$$\text{SRF}_{\text{ref}} = \frac{1}{N} \sum \text{SRF}_{\min(\text{Win_Len})} \quad (2)$$

where N indicates the number of Win_Len values. The cross-correlation coefficient between the SRF_{ref} and $\text{SRF}(\text{Inci_Ang}, \text{Win_Len})$ is then defined as:

$$\text{Coef}_{\text{SRF}}(\text{Inci_Ang}, \text{Win_Len}) = \text{CC}[\text{SRF}_{\text{ref}}, \text{SRF}(\text{Inci_Ang}, \text{Win_Len})], \quad (3)$$

where CC indicates the cross-correlation coefficient calculation. Finally, only the SRF that simultaneously satisfies (a) the smallest absolute amplitude at time zero and (b) the maximum Coef_{SRF} will be selected as the optimal SRF. The Inci_Ang and Win_Len values corresponding to this optimal SRF can either be used as a reference waveform for quality control or as input parameters that can be adapted to other deconvolution methods.

It is still necessary to perform quality control on the estimated SRFs from real data to remove any ambient noise and aliased waveforms. The results of the events with similar slowness at a single station should have good consistency, as has been fully demonstrated in previous receiver function studies (Kumar et al., 2006; Yuan et al., 2006), because the moveout corrected receiver functions reflects the structural information below the station (Kumar et al., 2010; Rost & Thomas, 2002). Therefore, the RMSE is applied for the quality control step. We first calculate the RMSE between each SRF and the average waveform at each station. We then reorder all the SRFs based on their RMSEs, with waveforms possessing clear and consistent Smp and SLP phases tending to be at the beginning of the sequence. Unlike Shen et al. (2019) used root mean square on the raw seismograms and SRF to do the quality control, we apply the RMSE to do the ordering and can select different proportions of the SRFs based on this reordered sequence to perform a linear summation. The best selection percentage can be determined by comparing the amplitudes of the Smp and SLP phases of the stacked waveforms that correspond to different data proportions. Here, we name this reordering method RMSE reordering and the best data proportion RMSE percentage.

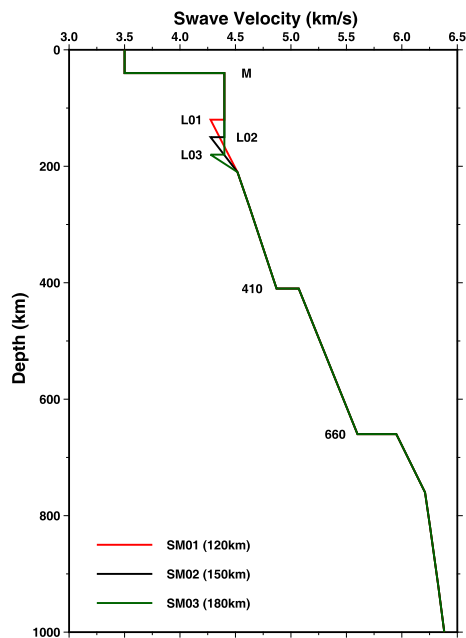


Figure 4. Models of S wave velocities for calculating the full wavefield synthetic seismograms. Three models SM01 (red), SM02 (black), and SM03 (dark green) are plotted in different colors. Compared with the IASP91 model, we simplified the crust to a single 40 km thick layer and only showed the upper 1,000 km of our models here.

3. Applications of the GC_SRF Strategy to Full Wavefield Synthetic Seismograms

3.1. Application to a One-Dimensional (1-D) Velocity Model

We first test the GC_SRF strategy on full wavefield synthetic seismograms using 1-D velocity models to demonstrate that this strategy can effectively calculate SRFs. Several attempts have been made previously to obtain synthetic full wavefield seismograms and synthetic SRFs (Shen et al., 2019; Yuan et al., 2006). Yuan et al. (2006) synthesized full wavefield seismograms via the reflectivity method (QSEIS, Wang, 1999); however, they obtained SRFs with only partial wavefield synthetic seismograms to avoid the deconvolution calculation. Although the partial wavefield synthetic seismograms possessed clear Sp converted phases, the observed field data consist of time series signals from the full wavefield. It is therefore necessary to rebuild the Sp phases from full wavefield synthetic seismograms to ensure the robustness of our proposed strategy.

The 1-D models that are employed in this study, which are constructed to a depth of 1,000 km based on IASP91 (Kennett & Engdahl, 1991), are shown in Figure 4, with the crust simplified to a single 40-km-thick layer. We introduce a 3% negative velocity jump at either 120 km (SM01), 150 km (SM02), or 180 km (SM03) depth to represent the LAB, following Yuan et al. (2006). We then employ the reflectivity method (Wang, 1999) to obtain full wavefield seismograms (Figure 5).

The synthetic seismograms that correspond to the three models in Figure 4 are shown in Figure 5. The travel time curves of the SLP phase (which represents the seismic phase converted at the LAB) for the three models are plotted as dashed lines (MOD01: red, MOD02: black; MOD03: green). The dashed blue lines represent the other theoretical phases from the SM02 model, whose LAB depth (150 km) is between those of the other two models. The various Sp converted phases cannot be recognized easily from the full wavefield synthetic seismograms. The details of the various Sp phases (including Smp, S410p, ScS410p, ScS660p, SKS410p, and SKS660p) are

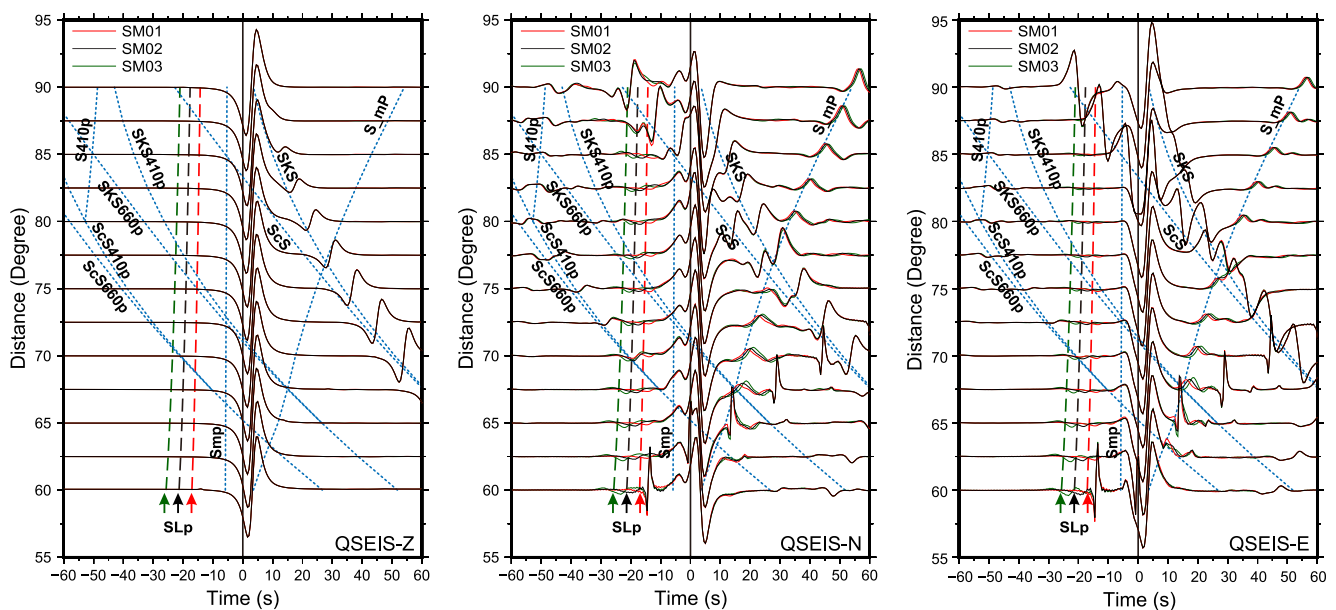


Figure 5. (a) Vertical, (b) North, and (c) East component full wavefield synthetic seismograms calculated by the reflectivity method (QSEIS, Wang, 1999) for the model shown in Figure 4. Time axis is aligned by S arrival time. The theoretical main phases are labeled and the arrival times are marked with blue dashed lines.

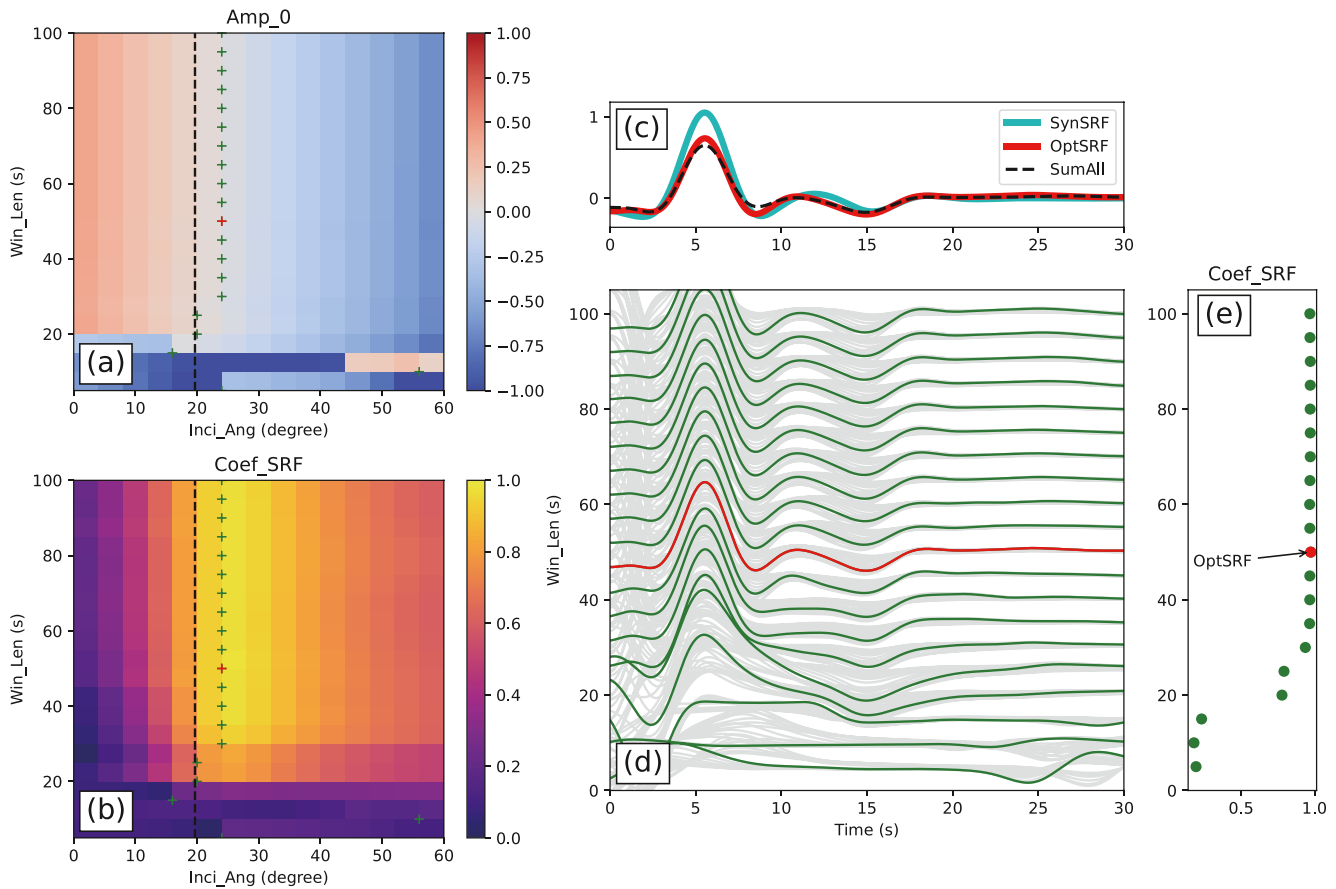


Figure 6. GC_SRF examples for SM01 ($t_S - t_{SLP} = 15.35$ s) with an epicentral distance of 75° . (a) Color map of the amplitude at time zero of the L component. (b) Color map of the Coef_{SRF} . (c) Comparison of Synthetic SRF (cyan), linear stacked SRF (black dashed), and the optimal SRF from GC_SRF. (d) All the SRFs corresponding to different Inci_Ang and Win_Len pairs (green curves show the optimal SRF for each Win_Len , the red curve represents the final optimal SRF, and the gray curves show the other SRFs). (e) Coef_{SRF} corresponding to all green and red crosses in (a) and (b).

difficult to identify on the N (Figure 5b) and Z (Figure 5a) components, as these phases are significantly weaker than either the ScS or SKS phases (Figure 5a). This is consistent with the full wave field synthetic seismogram shown in a previous study (Yuan et al., 2006), even though we use three modified velocity models in this study.

We apply the GC_SRF strategy to the full wavefield synthetic seismograms and obtain SRFs for all the Inci_Ang and Win_Len pairs. We present the GC_SRF results with an epicentral distance of 75° using model SM01 in Figure 6 to compare the differences among the three models (SM02: Figure S1; SM03: Figure S2 in Supporting Information S1). Figure 6a shows a colored map of the amplitudes at time zero on the L component (SRFL), whereas Figure 6b, Figures S1b, and S2b in Supporting Information S1 show Coef_{SRF} for all the parameter pairs. The dashed black line in Figure 6a indicates the incident angles of the S phase that are calculated by the TauP Toolkit (Crotwell et al., 1999), and the green crosses represent the position with the lowest amplitude; here the optimal SRF for each Win_Len value is selected where there is a polarity change in the waveform. Figure 6b shows a colored map of Coef_{SRF} , with the dashed line and green crosses representing the same variables as those in Figure 6a. The red crosses in these figures indicate the final optimal SRFs. The waveforms of all the SRFs in Figure 6d are shown as solid gray curves, and the waveforms that correspond to the optimal SRFs for each Win_Len value are shown as solid green curves. We also show the Coef_{SRF} corresponding to all the green and red waveforms in Figure 6e. The red curves in Figure 6d and the red crosses in Figure 6e indicate the optimal SRF (with the max Coef_{SRF}). Examples for models SM02 and SM03 are shown in Figures S1 and S2 in Supporting Information S1, respectively.

To present the efficiency of our proposed GC_SRF strategy, we calculate the theoretical synthetic SRFs using the three models (cyan curves in Figure 6c) via the propagator matrix method (Haskell, 1962). This method is

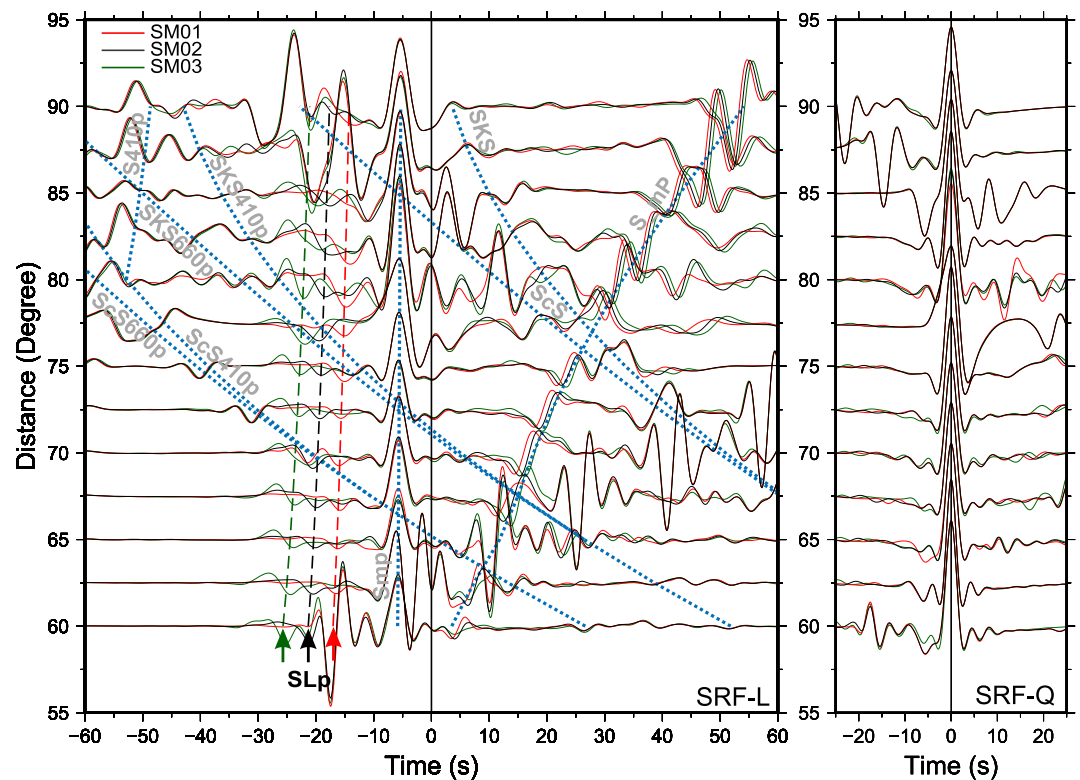


Figure 7. SRFs as a function of epicentral distances. The converted “p” phases are labeled, including Smp, SLP, S410p, ScS410p, ScS660p, SKS410p, and SKS660p. The theoretical arrival times of the main phases are marked with blue dashed lines. (a) Deconvolved L component (SRFL). (b) Deconvolved Q component (SRFQ).

efficient in obtaining the P- and SV-wave responses of a horizontally isotropic layered medium, which is often compared with the observed SRF (Niu & Kawakatsu, 1996; Randall, 1989; Vinnik et al., 2001). The dashed black waveform in Figure 6c is the linear stack of the SRFs that correspond to all the parameter pairs, whereas the red waveform corresponds to the optimal SRF. The optimal SRFs are in good agreement with the theoretical synthetic SRFs for the different models (Figure 6c, and Figures S1c and S2c in Supporting Information S1). These tests demonstrate the stability and reproducibility of the GC_SRF strategy. We then plot the optimal SRFs (SRFL) as a function of epicentral distance in Figure 7a.

The synthetic tests for the 1-D velocity model indicate that the GC_SRF strategy can successfully recover the Sp converted phases (see Figure 7). Notably, the Q-component (SRFQ) plot in Figure 7c has been suggested to reflect information on the earthquake sources (Kawakatsu et al., 2009; Vinnik et al., 2004), and this illustration has been deployed in previous studies (Geissler et al., 2010; Sodoudi et al., 2006). It is also evident that the Smp seismic phase is highly consistent at 5 s for the three models, as they all possess the same crustal thickness. Other notable features are the significant time shifts in the SLP phases for the three models and the fit of the peaks of the SLP phases to the theoretical travel time (see Table S1 in Supporting Information S1) within a certain range of epicentral distances (60°–80°). Furthermore, the results demonstrate that many other Sp phases, such as S410p, ScS410p, ScS660p, SKS410p, and SKS660p, can be rebuilt without artifacts.

3.2. Application to a Two-Dimensional (2-D) Velocity Model and Post-stack Migration

The robustness of the imaged discontinuities needs to be further demonstrated to ensure that a reliable lithospheric thickness is obtained; we therefore perform a resolution test for the 2-D case via forward modeling. We first construct a 2-D velocity model that is modified from IASP91 (Figure 8a) and calculate the full wavefield seismograms for a pseudo profile using 10 stations by QSEIS (Wang, 1999). The GC_SRF strategy is then used to calculate SRFs. A wave equation-based post-stack migration method (Chen et al., 2005a, 2005b) is employed for this resolution test. The moveout-corrected SRFs are first processed using time-domain common

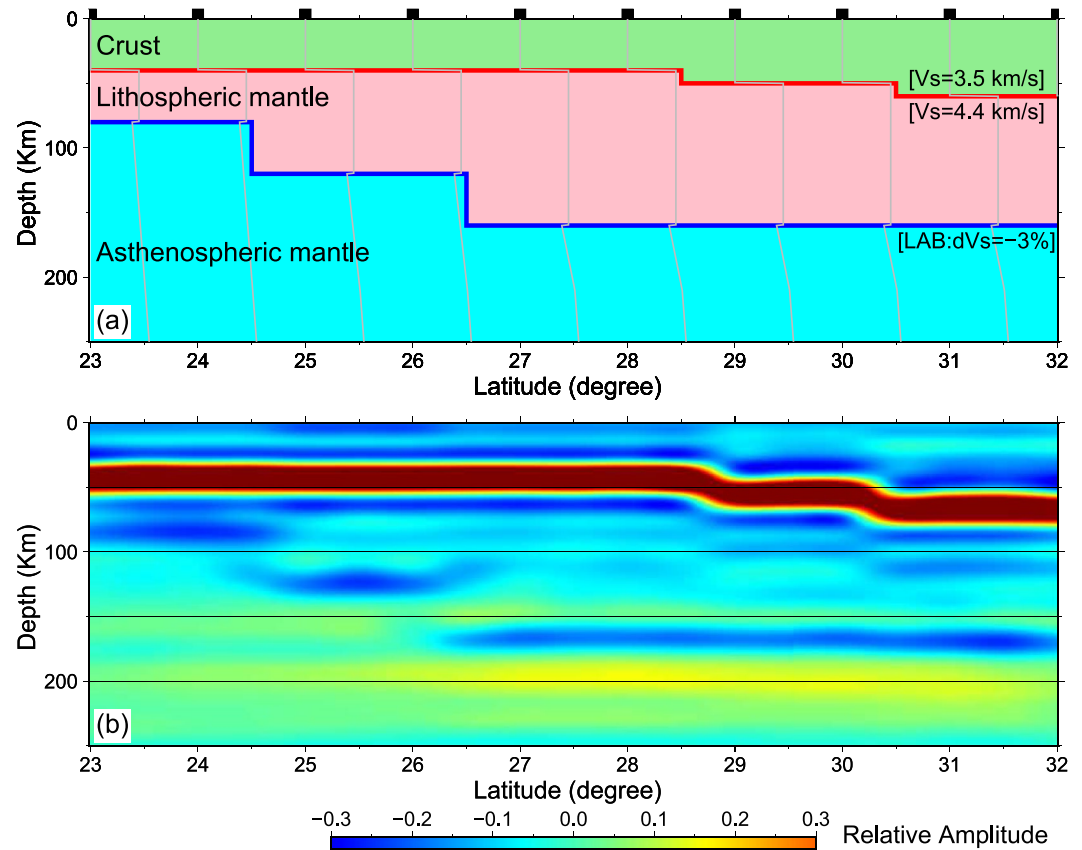


Figure 8. Synthetic test for a 2-D velocity model. (a) Synthetic velocity model modified from IASP91. The black boxes on the top show the pseudo stations where the 1-D velocity curves are plotted in gray. The red line indicates the Moho discontinuity, and the blue line represents the lithosphere–asthenosphere boundary (LAB) discontinuity. Velocity changes at discontinuities are labeled. (b) Post-stack migrated image of the GC_SRF results. The cutoff frequency limit is set to be 0.05–0.25 Hz.

conversion-point (CCP) stacking, and the stacked SRFs are subsequently processed using frequency-domain backward wavefield extrapolation to obtain the migrated images (Chen, 2009; Chen et al., 2009). We use rectangular stacking bins when performing CCP stacking. The bin width, which is perpendicular to the profile, is set to 200 km, whereas the bin length, which is parallel to the profile, varies with depth and data coverage. The modeling results (Figure 8b) show that the interface morphology in the theoretical velocity model can be recovered by migrating the SRF obtained by the GC_SRF strategy. The resolution test also indicates that the GC_SRF strategy is capable of obtaining reliable SRFs without artificial interference.

4. Distinct Lateral Variations of Lithospheric Thickness in Southeastern Tibet

It is necessary to test this strategy in a given region to validate its applicability and feasibility in LAB detection. Here we apply the GC_SRF strategy to seismic stations in southeastern Tibet. This area is adjacent to the Sichuan Basin in the east, and spans the Tengchong Volcano region and Permian Emeishan Large Igneous Province. Furthermore, this area is widely believed to possess channels that promote the eastward escape of materials from the Qinghai-Tibet Plateau (Molnar & Tapponnier, 1975; Tapponnier et al., 1982). Several large-scale geophysical investigations have previously been conducted across this region, including surface-wave tomography (e.g., Huang et al., 2013; Yao, 2020; Yao et al., 2008), body-wave tomography (e.g., Lei et al., 2014; Lei & Zhao, 2016), and PRF imaging (e.g., Xu et al., 2013; Yang et al., 2017).

Previous seismic anisotropy revealed remarkable changes in the south and north of southeastern Tibet (e.g., Lev et al., 2006). Recent Rayleigh-wave tomographic results have shown that a high-velocity anomaly is present at the LAB depth under the Chuandian region (Fu et al., 2017), whereas a body-wave tomographic study (Huang

et al., 2019) has revealed a low-velocity feature at the same depth range. Deng et al. (2021) obtained an independent constraint on the architecture via body-wave attenuation tomography, which suggested that the Sichuan Basin and Chuandian region possess the same extremely low attenuation structure. The Sichuan Basin belongs to an ancient craton and should have a relatively thick lithosphere, whereas Tengchong Volcano should have a relatively thin lithospheric thickness due to the underlying hot mantle (Deng & Tesauro, 2016; Sun et al., 2013). It is generally believed that a low velocity (Lei et al., 2009), high attenuation (Byrnes et al., 2019), and low effective elastic thickness (Chen et al., 2013) correspond to a thin lithosphere, whereas a high velocity, low attenuation, and high effective elastic thickness correspond to a thick lithosphere. However, the lithospheric thickness in this region remains unresolved. Although a few traditional receiver function methods have been used to determine the LAB depth distribution (Hu et al., 2011; Zhang et al., 2010, 2018) in this region, the results are hard to reproduce because they have quite different values, which may be due to artificial interference, even though they follow a similar pattern. Therefore, a robust and quantitative analysis of the lithospheric thickness in this region is of great significance for understanding its tectonic evolution.

4.1. GC_SRF-Based Data Processing

The analyzed teleseismic S waveform data were collected from 59 permanent stations between 96°–111°E and 22°–35°N (Figure 9) during the January 2010–December 2015 period (Zheng et al., 2010). We select teleseismic S waveforms from $M_s \geq 5.5$ earthquakes that occurred at epicentral distances of 50°–90° and possessed SNR_H greater than 5 for the GC_SRF approach. We obtain 18,239 SRFs with clear S_p phases from 879 seismic events after the preprocessing steps (see Methods section) and deconvolution.

We then reverse the time axis and performed RMSE reordering, followed by CCP stacking and migration. Different RMSE percentages (5%–100%) are tested in our estimations, with an example from station SC.MGU shown in Figure 10. Figures 10a and 10b show the SRFs before and after RMSE reordering, respectively, Figure 10c shows the change in RMSE with an index number, and Figures 10d and 10e show the stacked waveforms for different RMSE percentages. These two latter figures show that the RMSE percentage directly affects the amplitudes of both the S_{mp} and S_{lp} phases. Previous studies (Abt et al., 2010; Farra & Vinnik, 2000; Hansen et al., 2009) have indicated that a consistent and robust S_{mp} phase can be considered the premise for discussing the S_{lp} phase. After comparing other percentages, the selection of 30% ensures that the S_{lp} seismic phase can be significantly distinguished under the condition that the S_{mp} phase is as clear as possible. We finally choose the SRF data set with a 30% RMSE percentage for the CCP stacking and migration steps to ensure the reliability of the stacked waveform.

4.2. Post-Stack Migration Results in Southeastern Tibet

Post-stack migration is performed in the same way as that in the 2-D synthetic test. A velocity model that is based on IASP91 and the adjacent crustal structure (Yao, 2020) was used to calculate the delay times and piercing points, and perform the frequency-domain wavefield extrapolation. We separately select 0.03 and 0.05 Hz as the lower cutoff frequency limits (Zhang et al., 2018, 2019) and 0.2 and 0.25 Hz as the upper cutoff frequency limits to reduce the noise and illuminate the LAB depths.

The most prominent features in the CCP cross-section are the positive Moho phases (red-filled seismic waveforms in Figure 11a) at approximately 5–8 s, which can be continuously traced along the section. There are discontinuous negative phases (cyan-filled waveforms in Figure 11a) between approximately 10 and 25 s under the shallow positive Moho phase conversions. The post-stack migration results for different frequency contents, 0.03–0.2 Hz (Figures 11b), 0.03–0.25 Hz (Figure 11c), and 0.05–0.25 Hz (Figure 11d), possess discontinuity patterns that are similar to those in the CCP image (Figure 11a). The discontinuous negative (blue) layer exhibits larger variations at depth than the overlying continuous positive (red) layer.

4.3. Geodynamic Implications of the Lithospheric Structure

It is known that the S_{lp} phase is usually submerged in the S_{mp} sidelobe, as discussed in previous studies (Kind et al., 2020; Kumar et al., 2012; Li et al., 2007; Shen et al., 2019). We evaluate the robustness of the Moho and LAB depths using the criteria proposed by Zhang et al. (2018) and we only discuss the primary characteristics

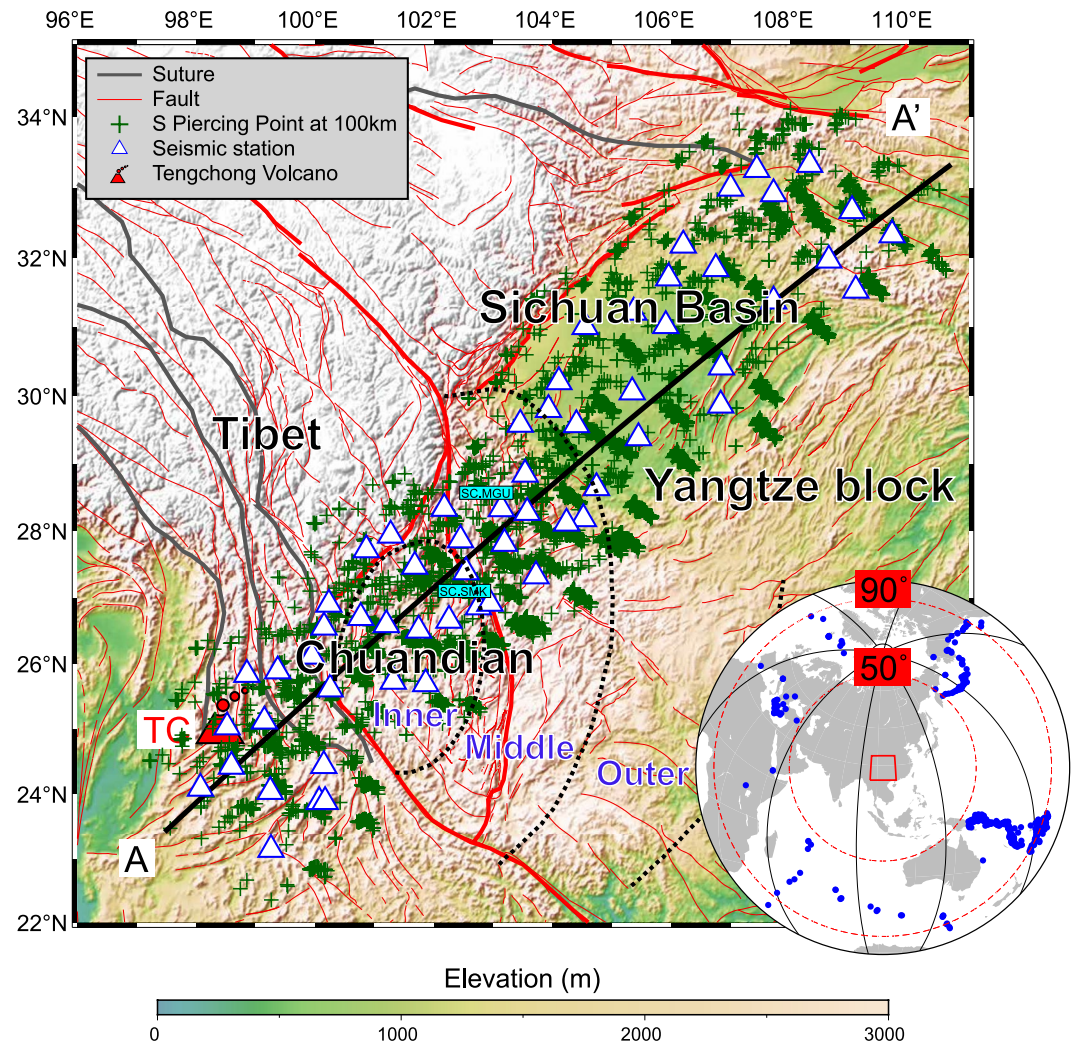


Figure 9. Topography of southeastern Tibet and adjacent regions. White triangles with blue lines represent the 59 stations used in this study. The black solid line represents the location of the migration profile A-A'. Dark-green crosses mark the piercing points of the corresponding SRFs at 100 km. Red lines indicate faults. Brown lines represent sutures. Black dashed arcs outline the inner, middle, and outer zones of the Permian Emeishan Large Igneous Province. Abbreviations: TC, Tengchong Volcano.

in this section. We carefully determine the negative phase that is adjacent to the Moho as the LAB signal (SLp phase), which is traced by the dashed gray line in Figure 11a. However, whether the negative phase after Moho can be interpreted as the mid-lithospheric discontinuities (MLD) or LAB, such as the observation beneath the North China Craton (Chen et al., 2014; Sun & Kennett, 2017), is a key problem. In order to illustrate such an issue in our results, we make several synthetic tests in Figure S3 in Supporting Information S1, which present how the sidelobe influence NVG signals with different LAB depths. Then we compare the negative phases beneath the Sichuan basin, the Tengchong Volcano and estimated sidelobes in Figure S4 in Supporting Information S1, and validate that the strong negative phase after Smp phase beneath the Tengchong Volcano is a combination of sidelobe and NVG signal, and the negative phase between Smp phase and SLp phase beneath the Sichuan Basin is also a combination of sidelobe and NVG signal (Text S1 in Supporting Information S1). Hence we interpret the negative phase under the Tengchong Volcano as the LAB, the shallow visible strong negative phase below Moho under the Sichuan Basin as the MLD.

The upper-crustal positive velocity gradient (PVG) is widely interpreted to be the result of thick sediment cover, as observed in other basins (Chen et al., 2009; Li et al., 2007; Mohsen et al., 2011; Tao et al., 2014). Recent

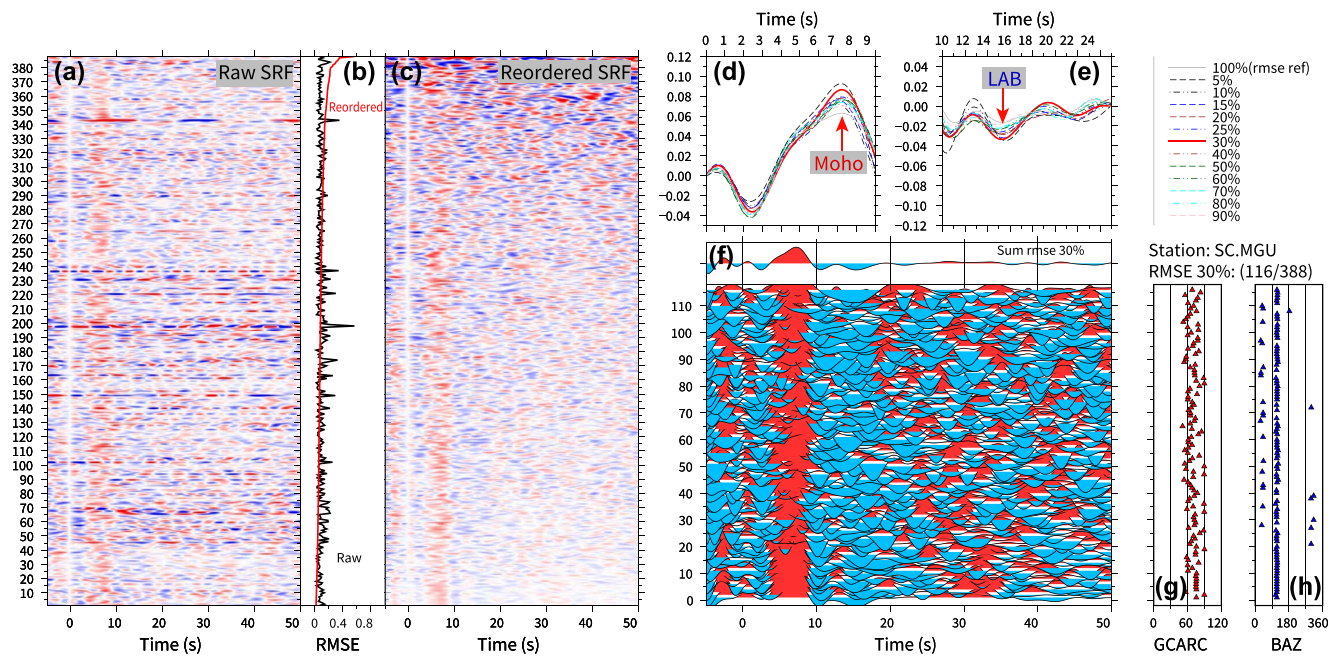


Figure 10. The reordered SRFs based on RMSE at station SC.MGU. (a) Raw SRFs after deconvolution. (b) The RMSE values corresponding to each SRF. The black line shows the RMSE of the raw sequence, while the red is for reordered ones. (c) Reordered SRFs based on RMSE. (d) and (e) Present the Smp phase and SLP phase corresponding to different RMSE percentages. (f) SRFs of 30% RMSE percentage and the top waveform indicates the summation of these waveforms. The epicentral distance (GCARC) and back-azimuth (BAZ) for each event as well as the total number of SRFs are listed in (g and h).

research has suggested that the sediment cover across the Sichuan Basin ranges from 6 to 13 km in thickness (Xia et al., 2021). Our results indicate a discontinuous distribution pattern of the PVG that is concentrated mainly in the Sichuan Basin area. We make the synthetic tests (see Figure S5 in Supporting Information S1) with varying the upper crustal PVG depths, which indicate a 5 km PVG can fit stacked SRF beneath the Sichuan Basin best (Text S2 in Supporting Information S1). Notably, the spatial distribution range of the PVG is also consistent with the range of low elevations within the basin area, we therefore interpret the PVG to represent the basement of the Sichuan Basin sediments.

A thick crust lies beneath the Sichuan Basin (~50 km), whereas a thin crust lies beneath Tengchong Volcano (~40 km), with the thickest crust observed in the Chuandian region (~60 km; Figure 11b). This pattern is consistent with comprehensive geophysical investigations that revealed magmatic underplating beneath the Chuandian region (Chen et al., 2015; Deng et al., 2016; Xu et al., 2014), even though the SRF uncertainties are larger than the uncertainties associated with the PRF and active seismic results. Furthermore, our study highlights a lithospheric thickness of ~160 km beneath the Sichuan Basin, with a thickness of ~90 km beneath the Tengchong Volcano. The discontinuity patterns of the crust and lithosphere are consistent with previous SRF studies (Hu et al., 2011; Peng et al., 2021; Zhang et al., 2015) in the same region; however, our results are obtained without artificial interference. Previous studies have employed receiver function, ambient noise tomography, and body-wave and surface-wave tomography methods to clarify both the Moho discontinuities and LAB near our study region (Wang et al., 2021; Wei et al., 2022; Zhou et al., 2012), with each of these studies suggesting a thin crust and thin lithosphere beneath Tengchong Volcano. A thick (150–180 km) lithosphere that underlies a crustal lid (35–50 km) has also been observed beneath the Sichuan Basin (Wang et al., 2018; Zhang et al., 2010, 2018), with the thick lithosphere beneath the basin being a typical characteristic of this ancient craton (Li et al., 2021; Wang et al., 2022).

However, the LAB beneath the Chuandian region is not clear compared with that of the Sichuan Basin and Tengchong Volcano. Permian Emeishan flood basalts have been emplaced beneath the Chuandian region, with the lack of a detectable LAB aligning directly beneath the inner zones of the Permian Emeishan Large Igneous Province. The mantle plume model is a popular approach for explaining the geophysical and geochemical observations (Chen et al., 2015; Deng et al., 2016; Li et al., 2021; Xu et al., 2007) in large igneous provinces.

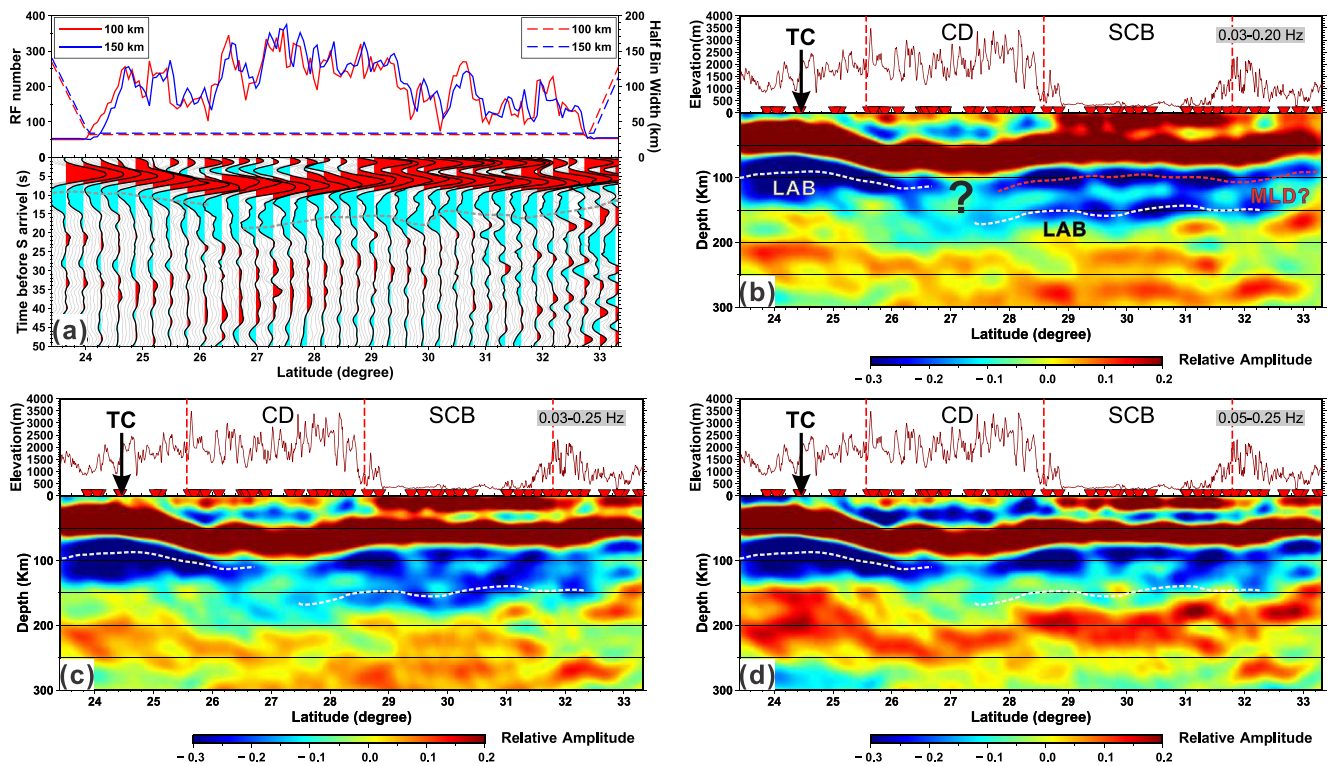


Figure 11. Common conversion point (CCP) stacking profile and post-stack migration image profile along A-A' shown in Figure 7. (a) Stacked sections of S receiver functions (0.03–0.5 Hz) after moveout correction. The coherent negative SLP phase is traced by gray dashed lines. The top panel presents the RF number (solid lines) and half width (dashed lines) for each bin. (b–d) Post-stack migration SRF images. Different frequency contributions of the data are considered in imaging: (b) 0.03–0.2 Hz; (c) 0.03–0.25 Hz; (d) 0.05–0.25 Hz. On each top panel, the red solid lines show the topography, and the red dashed lines represent geological boundaries. The white dashed lines on the bottom panel of (b–d) indicate lithosphere–asthenosphere boundary (LAB) while the red dashed line in (b) presents the possible mid-lithospheric discontinuities (MLDs). Abbreviations: CD, Chuandian; SCB, Sichuan Basin; TC, Tengchong Volcano.

The plume head could undergo strong changes and erode the overlying lithosphere owing to high temperatures and push it upward, with this being a common type of lithospheric thinning caused by a rising plume (Burov et al., 2007; Hawkesworth et al., 2017); this phenomenon is known as plume-induced lithospheric destruction. However, the lithosphere could undergo downgrowth through cooling when the plume was gone, as demonstrated in North America (Hawkesworth et al., 2017; Yuan & Romanowicz, 2010). A recent study has also shown that the plume could also reocratize the lithosphere, mainly through compositional changes, as demonstrated in Arctic Canada (Liu, Pearson, et al., 2021). This newly generated LAB possesses a smaller velocity jump than the old LAB, such that its amplitude is smaller than that beneath the Sichuan Basin. We therefore suggest that the unclear LAB beneath the Chuandian region indicates regrowth of the modified lithosphere owing to the recovery after the mantle plume processes, which in turn produced the unique seismic velocity pattern, low attenuation, and high resistivity in this region (Deng et al., 2021; Li et al., 2020).

5. Conclusion

We propose a new strategy, the GC_SRF strategy, to obtain the lithospheric thickness without artificial interference. We precisely determine the parameters in obtaining SRFs and avoided possible artifacts by employing grid search and correlation analysis. The 30% RMSE is employed to do the quality control. The synthetic tests indicate that this GC_SRF strategy can obtain reliable SRFs from full waveform seismograms. Our application of the GC_SRF strategy in southeastern Tibet demonstrates this strategy yields excellent statistical consistency in single-station analysis. The migrated image shows that the Chuandian region possesses the thickest crust in the study area, followed by the Sichuan Basin, with the thinnest crust located beneath Tengchong Volcano. Furthermore, a thick lithosphere beneath the Sichuan Basin (~160 km) and a thin lithosphere beneath Tengchong Volcano (~90 km) have been imaged. Another notable finding is that the LAB signal is unclear beneath

the Chuandian region, which is interpreted to indicate lithospheric regrowth after modification of the Emeishan mantle plume. These combined results suggest that this new strategy is suitable for obtaining SRFs and constraining the lithospheric thickness without artificial interference. This strategy can be widely applied to other regions for obtaining the lithospheric thickness and advancing our understanding of lithospheric evolution. The influences of different velocity jumps and sharpness of LAB on the SRF amplitude warrant future research.

Data Availability Statement

The raw data used to reproduce the S-wave receiver functions (SRFs) of Kumar et al. (2006) can be downloaded at the IRIS Data Management Center (XR, INDEPTH III, https://doi.org/10.7914/SN/XR_1997). The seismic raw data in southeastern Tibet can be available by request through the Data Management Centre of the China National Seismic Network at the Institute of Geophysics. The data to produce SRFs and the obtained SRFs generated by GC_SRF in southeastern Tibet, and the source code of SX_Deconv can be accessed at <https://doi.org/10.6084/m9.figshare.19471061>.

References

- Abt, D. L., Fischer, K. M., French, S. W., Ford, H. A., Yuan, H., & Romanowicz, B. (2010). North American lithospheric discontinuity structure imaged by Ps and Sp receiver functions. *Journal of Geophysical Research*, *115*(B9), B09301. <https://doi.org/10.1029/2009JB006914>
- Bijwaard, H., & Spakman, W. (2000). Non-linear global P-wave tomography by iterated linearized inversion. *Geophysical Journal International*, *141*(1), 71–82. <https://doi.org/10.1046/j.1365-246X.2000.00053.x>
- Bostock, M. G. (1999). Seismic imaging of lithospheric discontinuities and continental evolution. *Lithos*, *48*(1–4), 1–16. [https://doi.org/10.1016/S0024-4937\(99\)00020-1](https://doi.org/10.1016/S0024-4937(99)00020-1)
- Buck, W. (1991). Modes of continental lithospheric extension. *Journal of Geophysical Research*, *96*(B12), 20161–20178. <https://doi.org/10.1029/91JB01485>
- Burov, E., Guillou-Frotier, L., d'Acremont, E., Le Pourhiet, L., & Cloetingh, S. (2007). Plume head-lithosphere interactions near intra-continental plate boundaries. *Tectonophysics*, *434*(1–4), 15–38. <https://doi.org/10.1016/j.tecto.2007.01.002>
- Byrnes, J. S., Bezada, M., Long, M. D., & Benoit, M. H. (2019). Thin lithosphere beneath the central Appalachian Mountains: Constraints from seismic attenuation beneath the MAGIC array. *Earth and Planetary Science Letters*, *519*, 297–307. <https://doi.org/10.1016/j.epsl.2019.04.045>
- Chen, B., Chen, C., Kaban, M. K., Du, J., Liang, Q., & Thomas, M. (2013). Variations of the effective elastic thickness over China and surroundings and their relation to the lithosphere dynamics. *Earth and Planetary Science Letters*, *363*, 61–72. <https://doi.org/10.1016/j.epsl.2012.12.022>
- Chen, L. (2009). Lithospheric structure variations between the eastern and central North China Craton from S- and P-receiver function migration. *Physics of the Earth and Planetary Interiors*, *173*(3–4), 216–227. <https://doi.org/10.1016/j.pepi.2008.11.011>
- Chen, L., Cheng, C., & Wei, Z. (2009). Seismic evidence for significant lateral variations in lithospheric thickness beneath the central and Western North China Craton. *Earth and Planetary Science Letters*, *286*(1–2), 171–183. <https://doi.org/10.1016/j.epsl.2009.06.022>
- Chen, L., Jiang, M., Yang, J., Wei, Z., Liu, C., & Ling, Y. (2014). Presence of an intralithospheric discontinuity in the central and Western North China Craton: Implications for destruction of the craton. *Geology*, *42*(3), 223–226. <https://doi.org/10.1130/G35010.1>
- Chen, L., Wen, L., & Zheng, T. (2005a). A wave equation migration method for receiver function imaging: 1. Theory. *Journal of Geophysical Research*, *110*(B11). <https://doi.org/10.1029/2005JB003665>
- Chen, L., Wen, L., & Zheng, T. (2005b). A wave equation migration method for receiver function imaging: 2. Application to the Japan subduction zone. *Journal of Geophysical Research*, *110*(B11). <https://doi.org/10.1029/2005JB003666>
- Chen, Y., Xu, Y., Xu, T., Si, S., Liang, X., Tian, X., et al. (2015). Magmatic underplating and crustal growth in the Emeishan Large Igneous Province, SW China, revealed by a passive seismic experiment. *Earth and Planetary Science Letters*, *432*, 103–114. <https://doi.org/10.1016/j.epsl.2015.09.048>
- Chu, R., Zhu, L., & HelMBERGER, D. V. (2009). Determination of earthquake focal depths and source time functions in central Asia using teleseismic P waveforms. *Geophysical Research Letters*, *36*(17), L17317. <https://doi.org/10.1029/2009GL039494>
- Crotwell, P. H., Owens, T. J., & Ritsema, J. (1999). The TauP toolkit: Flexible seismic travel-time and ray-path utilities. *Seismological Research Letters*, *70*(2), 154–160. <https://doi.org/10.1785/gssrl.70.2.154>
- Davies, J. H., & Von Blanckenburg, F. (1995). Slab breakoff—A model of lithosphere detachment and its test in the magmatism and deformation of collisional orogens. *Earth and Planetary Science Letters*, *129*(1–4), 85–102. [https://doi.org/10.1016/0012-821x\(94\)00237-s](https://doi.org/10.1016/0012-821x(94)00237-s)
- Deng, Y., Byrnes, J. S., & Bezada, M. (2021). New insights into the heterogeneity of the lithosphere-asthenosphere system beneath south China from teleseismic body-wave attenuation. *Geophysical Research Letters*, *48*(6). <https://doi.org/10.1029/2020GL091654>
- Deng, Y., Chen, Y., Wang, P., Essa, K., Xu, T., Liang, X., & Badal, J. (2016). Magmatic underplating beneath the Emeishan large igneous province (South China) revealed by the COMGRA-ELIP experiment. *Tectonophysics*, *672*, 16–23. <https://doi.org/10.1016/j.tecto.2016.01.039>
- Deng, Y. F., & Tesauero, M. (2016). Lithospheric strength variations in Mainland China: Tectonic implications. *Tectonics*, *35*(10), 2313–2333. <https://doi.org/10.1002/2016tc004272>
- Farra, V., & Vinnik, L. (2000). Upper mantle stratification by P and S receiver functions. *Geophysical Journal International*, *141*(3), 699–712. <https://doi.org/10.1046/j.1365-246x.2000.00118.x>
- Fichtner, A., Kennett, B. L. N., Igel, H., & Bunge, H. P. (2009). Full seismic waveform tomography for upper-mantle structure in the Australasian region using adjoint methods. *Geophysical Journal International*, *179*(3), 1703–1725. <https://doi.org/10.1111/j.1365-246X.2009.04368.x>
- Fischer, K. M., Ford, H. A., Abt, D. L., & Rychert, C. A. (2010). The lithosphere-asthenosphere boundary. In R. Jeanloz & K. Freeman (Eds.), *Annual review of Earth and planetary sciences* (Vol. 38, pp. 551–575). <https://doi.org/10.1146/annurev-earth-040809-152438>
- Fischer, K. M., Rychert, C. A., Dalton, C. A., Miller, M. S., Beghein, C., & Schutt, D. L. (2020). A comparison of oceanic and continental mantle lithosphere. *Physics of the Earth and Planetary Interiors*, *309*, 106600. <https://doi.org/10.1016/j.pepi.2020.106600>
- Fu, Y. V., Gao, Y., Li, A., Li, L., & Chen, A. (2017). Lithospheric structure of the southeastern margin of the Tibetan Plateau from Rayleigh wave tomography. *Journal of Geophysical Research-Solid Earth*, *122*(6), 4631–4644. <https://doi.org/10.1002/2016JB013096>

Acknowledgments

The authors acknowledge the Data Management Centre of the China National Seismic Network at the Institute of Geophysics (<https://doi.org/10.11998/SeisDmc/SN>, <http://www.seisdmc.ac.cn/>; Zheng et al., 2010) for providing part seismic raw data, and Professor Rongjiang Wang of Helmholtz-Centre Potsdam-German Research Centre for Geosciences (GFZ) for providing QSEIS (Wang, 1999). The authors also thank Professor Vinnik L.P., Xiaohui Yuan, Qingju Wu, Qimin Liu, and Qiang Xu for their valuable discussions. The authors appreciate Zhuo Xiao, Junliu Suwen, and the colleagues at office 724A in GIGCAS for their help and advice. Constructive comments from Editors, Dr. Rob Porritt, and other two anonymous reviewers have greatly improved this manuscript. This work is funded by National Science Foundation of China (41874106, 42104103, 42021002), and Youth Innovation Promotion Association CAS (YIPA2018385). Some figures are plotted with matplotlib (Hunter, 2007) and Generic Mapping Tools (Wessel & Smith, 1995; Wessel et al., 2019).

- Geissler, W. H., Sodoudi, F., & Kind, R. (2010). Thickness of the central and eastern European lithosphere as seen by S receiver functions. *Geophysical Journal International*, 181(2), 604–634. <https://doi.org/10.1111/j.1365-246X.2010.04548.x>
- Hansen, S. E., Nyblade, A. A., Heeszel, D. S., Wiens, D. A., Shore, P., & Kanao, M. (2010). Crustal structure of the Gamburtsev Mountains, East Antarctica, from S-wave receiver functions and Rayleigh wave phase velocities. *Earth and Planetary Science Letters*, 300(3–4), 395–401. <https://doi.org/10.1016/j.epsl.2010.10.022>
- Hansen, S. E., Nyblade, A. A., Julia, J., Dirks, P. H. G. M., & Durrheim, R. J. (2009). Upper-mantle low-velocity zone structure beneath the Kaapvaal craton from S-wave receiver functions. *Geophysical Journal International*, 178(2), 1021–1027. <https://doi.org/10.1111/j.1365-246X.2009.04178.x>
- Haskell, N. (1962). Crustal reflection of plane P and SV waves. *Journal of Geophysical Research*, 67(12), 4751–. <https://doi.org/10.1029/JZ067i012p04751>
- Hawkesworth, C. J., Cawood, P. A., Dhuime, B., & Kemp, T. I. S. (2017). Earth's continental lithosphere through time. In R. Jeanloz & K. H. Freeman (Eds.), *Annual review of Earth and planetary sciences* (Vol. 45, pp. 169–198). <https://doi.org/10.1146/annurev-earth-063016-020525>
- Hopper, E., & Fischer, K. (2015). The meaning of midlithospheric discontinuities: A case study in the northern US craton. *Geochemistry, Geophysics, Geosystems*, 16(12), 4057–4083. <https://doi.org/10.1002/2015GC006030>
- Houseman, G. A., McKenzie, D. P., & Molnar, P. (1981). Convective instability of a thickened boundary-layer and its relevance for the thermal evolution of continental convergent belts. *Journal of Geophysical Research*, 86(Nb7), 6115–6132. <https://doi.org/10.1029/JB086iB07p06115>
- Hu, J., Xu, X., Yang, H., Wen, L., & Li, G. (2011). S receiver function analysis of the crustal and lithospheric structures beneath eastern Tibet. *Earth and Planetary Science Letters*, 306(1–2), 77–85. <https://doi.org/10.1016/j.epsl.2011.03.034>
- Huang, Z., Li, H.-Y., & Xu, Y. (2013). Lithospheric S-wave velocity structure of the North-South Seismic Belt of China from surface wave tomography. *Chinese Journal of Geophysics-Chinese Edition*, 56(4), 1121–1131. <https://doi.org/10.6038/cjg20130408>
- Huang, Z., Wang, L., Xu, M., Zhao, D., Mi, N., & Yu, D. (2019). P and S wave tomography beneath the SE Tibetan Plateau: Evidence for lithospheric delamination. *Journal of Geophysical Research-Solid Earth*, 124(10), 10292–10308. <https://doi.org/10.1029/2019JB017430>
- Hunter, J. D. (2007). Matplotlib: A 2D graphics environment. *Computing in Science & Engineering*, 9(3), 90–95. <https://doi.org/10.1109/MCSE.2007.55>
- Kawakatsu, H., Kumar, P., Takei, Y., Shinohara, M., Kanazawa, T., Araki, E., & Suyehiro, K. (2009). Seismic evidence for sharp lithosphere-asthenosphere boundaries of oceanic plates. *Science*, 324(5926), 499–502. <https://doi.org/10.1126/science.1169499>
- Kennett, B., & Engdahl, E. (1991). Traveltimes for global earthquake location and phase identification. *Geophysical Journal International*, 105(2), 429–465. <https://doi.org/10.1111/j.1365-246X.1991.tb06724.x>
- Kind, R., Mooney, W. D., & Yuan, X. (2020). New insights into the structural elements of the upper mantle beneath the contiguous United States from S-to-P converted seismic waves. *Geophysical Journal International*, 222(1), 646–659. <https://doi.org/10.1093/gji/ggaa203>
- Kind, R., Yuan, X., & Kumar, P. (2012). Seismic receiver functions and the lithosphere-asthenosphere boundary. *Tectonophysics*, 536, 25–43. <https://doi.org/10.1016/j.tecto.2012.03.005>
- Kosarev, G., Kind, R., Sobolev, S. V., Yuan, X., Hanka, W., & Oreshin, S. (1999). Seismic evidence for a detached Indian lithospheric mantle beneath Tibet. *Science*, 283(5406), 1306–1309. <https://doi.org/10.1126/science.283.5406.1306>
- Kumar, P., Kind, R., & Yuan, X. (2010). Receiver function summation without deconvolution. *Geophysical Journal International*, 180(3), 1223–1230. <https://doi.org/10.1111/j.1365-246X.2009.04469.x>
- Kumar, P., Kind, R., Yuan, X., & Mechie, J. (2012). USArray receiver function images of the lithosphere-asthenosphere boundary. *Seismological Research Letters*, 83(3), 486–491. <https://doi.org/10.1785/gssrl.83.3.486>
- Kumar, P., Yuan, X., Kind, R., & Ni, J. (2006). Imaging the colliding Indian and Asian lithospheric plates beneath Tibet. *Journal of Geophysical Research*, 111(B6). <https://doi.org/10.1029/2005JB003930>
- Langston, C. (1979). Structure under Mount Rainier, Washington, inferred from teleseismic body waves. *Journal of Geophysical Research*, 84(NB9), 4749–4762. <https://doi.org/10.1029/JB084iB09p04749>
- Lei, J., Li, Y., Xie, F., Teng, J., Zhang, G., Sun, C., & Zha, X. (2014). Pn anisotropic tomography and dynamics under eastern Tibetan plateau. *Journal of Geophysical Research-Solid Earth*, 119(3), 2174–2198. <https://doi.org/10.1002/2013JB010847>
- Lei, J., & Zhao, D. (2016). Teleseismic P-wave tomography and mantle dynamics beneath Eastern Tibet. *Geochemistry, Geophysics, Geosystems*, 17(5), 1861–1884. <https://doi.org/10.1002/2016GC006262>
- Lei, J., Zhao, D., & Su, Y. (2009). Insight into the origin of the Tengchong intraplate volcano and seismotectonics in southwest China from local and teleseismic data. *Journal of Geophysical Research*, 114(B5), B05302. <https://doi.org/10.1029/2008JB005881>
- Lev, E., Long, M. D., & van der Hilst, R. D. (2006). Seismic anisotropy in Eastern Tibet from shear wave splitting reveals changes in lithospheric deformation. *Earth and Planetary Science Letters*, 251(3–4), 293–304. <https://doi.org/10.1016/j.epsl.2006.09.018>
- Levander, A., & Miller, M. S. (2012). Evolutionary aspects of lithosphere discontinuity structure in the Western U.S. *Geochemistry, Geophysics, Geosystems*, 13(7). <https://doi.org/10.1029/2012GC004056>
- Levinson, N. (1946). The wiener RMS (root mean square) error criterion in filter design and prediction. *Journal of Mathematics and Physics*, 25(4), 261–278. <https://doi.org/10.1002/sapm1946251261>
- Li, W., Chen, Y., Liang, X., & Xu, Y.-G. (2021). Lateral seismic anisotropy variations record interaction between Tibetan mantle flow and plume-strengthened yangtze craton. *Journal of Geophysical Research-Solid Earth*, 126(4). <https://doi.org/10.1029/2020JB020841>
- Li, X., Ma, X. B., Chen, Y., Xue, S., Varentsov, I. M., & Bai, D. H. (2020). A plume-modified lithospheric barrier to the southeastward flow of partially molten Tibetan crust inferred from magnetotelluric data. *Earth and Planetary Science Letters*, 548, 116493. <https://doi.org/10.1016/j.epsl.2020.116493>
- Li, X., Yuan, X., & Kind, R. (2007). The lithosphere-asthenosphere boundary beneath the Western United States. *Geophysical Journal International*, 170(2), 700–710. <https://doi.org/10.1111/j.1365-246X.2007.03428.x>
- Ligorria, J., & Ammon, C. (1999). Iterative deconvolution and receiver-function estimation. *Bulletin of the Seismological Society of America*, 89(5), 1395–1400. <https://doi.org/10.1785/BSSA0890051395>
- Liu, J., Pearson, D. G., Wang, L. H., Mather, K. A., Kjarsgaard, B. A., Schaeffer, A. J., et al. (2021). Plume-driven recretionization of deep continental lithospheric mantle. *Nature*, 592(7856), 732–736. <https://doi.org/10.1038/s41586-021-03395-5>
- Liu, L., Klemperer, S. L., & Blanchette, A. R. (2021). Western Gondwana imaged by S receiver-functions (SRF): New results on Moho, MLD (mid-lithospheric discontinuity) and LAB (lithosphere-asthenosphere boundary). *Gondwana Research*, 96, 206–218. <https://doi.org/10.1016/j.gr.2021.04.009>
- Liu, X., & Zhao, D. (2021). Seismic evidence for a plume-modified oceanic lithosphere-asthenosphere system beneath Cape Verde. *Geophysical Journal International*, 225(2), 872–886. <https://doi.org/10.1093/gji/ggab012>

- Long, M. D., Wagner, L. S., King, S. D., Evans, R. L., Mazza, S. E., Byrnes, J. S., et al. (2021). Evaluating models for lithospheric loss and intraplate volcanism beneath the central Appalachian Mountains. *Journal of Geophysical Research-Solid Earth*, 126(10). <https://doi.org/10.1029/2021JB022571>
- Mohsen, A., Asch, G., Mechie, J., Kind, R., Hofstetter, R., Weber, M., et al. (2011). Crustal structure of the Dead Sea Basin (DSB) from a receiver function analysis. *Geophysical Journal International*, 184(1), 463–476. <https://doi.org/10.1111/j.1365-246X.2010.04853.x>
- Mojaver, O. B., Darbyshire, F., & Dave, R. (2021). Lithospheric structure and flat-slab subduction in the northern Appalachians: Evidence from Rayleigh wave tomography. *Journal of Geophysical Research-Solid Earth*, 126(4). <https://doi.org/10.1029/2020JB020924>
- Molnar, P., & Tapponnier, P. (1975). Cenozoic Tectonics of Asia: Effects of a Continental Collision: Features of recent continental tectonics in Asia can be interpreted as results of the India-Eurasia collision. *Science*, 189(4201), 419–426. <https://doi.org/10.1126/science.189.4201.419>
- Niu, F. L., & Kawakatsu, H. (1996). Complex structure of mantle discontinuities at the tip of the subducting slab beneath Northeast China - a preliminary investigation of broadband receiver functions. *Journal of Physics of the Earth*, 44(6), 701–711. <https://doi.org/10.4294/jpe1952.44.701>
- Oppenheim, A. (1969). Speech analysis-synthesis system based on homomorphic filtering. *Journal of the Acoustical Society of America*, 45(2), 458–465. <https://doi.org/10.1121/1.1911395>
- Peng, H., Badal, J., Hu, J., Yang, H., & Liu, B. (2021). Lithospheric dynamics in the vicinity of the Tengchong volcanic field (southeastern margin of Tibet): An investigation using P receiver functions. *Geophysical Journal International*, 224(2), 1327–1344. <https://doi.org/10.1093/gji/ggaa517>
- Randall, G. (1989). Efficient calculation of differential seismograms for lithospheric receiver functions. *Geophysical Journal International*, 99(3), 469–481. <https://doi.org/10.1111/j.1365-246X.1989.tb02033.x>
- Rawlinson, N., & Fishwick, S. (2012). Seismic structure of the southeast Australian lithosphere from surface and body wave tomography. *Tectonophysics*, 572, 111–122. <https://doi.org/10.1016/j.tecto.2011.11.016>
- Reading, A., Kennett, B., & Sambridge, M. (2003). Improved inversion for seismic structure using transformed, S-wavevector receiver functions: Removing the effect of the free surface. *Geophysical Research Letters*, 30(19), 1981. <https://doi.org/10.1029/2003GL018090>
- Ritsema, J., van Heijst, H., & Woodhouse, J. (2004). Global transition zone tomography. *Journal of Geophysical Research*, 109(B2). <https://doi.org/10.1029/2003JB002610>
- Ritzwoller, M., Shapiro, N., Barmin, M., & Levshin, A. (2002). Global surface wave diffraction tomography. *Journal of Geophysical Research*, 107(B12), ESE4-1–ESE4-13. <https://doi.org/10.1029/2002JB001777>
- Robinson, E., & Treitel, S. (1976). Net downgoing energy and resulting minimum-phase property of downgoing waves. *Geophysics*, 41(6), 1394–1396. <https://doi.org/10.1190/1.1440689>
- Robinson, E., & Treitel, S. (2000). *Geophysical signal analysis*. Society of Exploration Geophysicists. <https://doi.org/10.1190/1.9781560802327>
- Rost, S., & Thomas, C. (2002). Array seismology: Methods and applications. *Reviews of Geophysics*, 40(3), 2-1–2-27. <https://doi.org/10.1029/2000RG000100>
- Shen, X., Kim, Y., Song, T.-R. A., & Lim, H. (2019). Data-oriented constraint on the interpretation of S receiver function and its application to observations of seismic discontinuities in the lithosphere-asthenosphere system. *Geophysical Journal International*, 219(1), 496–513. <https://doi.org/10.1093/gji/ggz316>
- Soudoufi, F., Kind, R., Hatzfeld, D., Priestley, K., Hanka, W., Wylegalla, K., et al. (2006). Lithospheric structure of the Aegean obtained from P and S receiver functions. *Journal of Geophysical Research*, 111(B12). <https://doi.org/10.1029/2005JB003932>
- Stammler, K. (1993). Seismichandler programmable multichannel data handler for interactive and automatic processing of seismological analyses. *Computers & Geosciences*, 19(2), 135–140. [https://doi.org/10.1016/0098-3004\(93\)90110-Q](https://doi.org/10.1016/0098-3004(93)90110-Q)
- Sun, W., & Kennett, B. (2017). Mid-lithosphere discontinuities beneath the Western and central north China craton. *Geophysical Research Letters*, 44(3), 1302–1310. <https://doi.org/10.1002/2016GL071840>
- Sun, Y. J., Dong, S. W., Zhang, H., Li, H., & Shi, Y. L. (2013). 3D thermal structure of the continental lithosphere beneath China and adjacent regions. *Journal of Asian Earth Sciences*, 62, 697–704. <https://doi.org/10.1016/j.jseaes.2012.11.020>
- Tao, K., Niu, F., Ning, J., Chen, Y. J., Grand, S., Kawakatsu, H., et al. (2014). Crustal structure beneath NE China imaged by NECESSArray receiver function data. *Earth and Planetary Science Letters*, 398, 48–57. <https://doi.org/10.1016/j.epsl.2014.04.043>
- Tape, C., Liu, Q., & Tromp, J. (2007). Finite-frequency tomography using adjoint methods—Methodology and examples using membrane surface waves. *Geophysical Journal International*, 168(3), 1105–1129. <https://doi.org/10.1111/j.1365-246X.2006.03191.x>
- Tapponnier, P., Peltzer, G., Ledain, A., Armijo, R., & Cobbold, P. (1982). Propagating extrusion tectonics in Asia - New insights from simple experiments with plasticine. *Geology*, 10(12), 611–616. [https://doi.org/10.1130/0091-7613\(1982\)10<611:PETIAN>2.0.CO;2](https://doi.org/10.1130/0091-7613(1982)10<611:PETIAN>2.0.CO;2)
- Thybo, H. (2006). The heterogeneous upper mantle low velocity zone. *Tectonophysics*, 416(1–4), 53–79. <https://doi.org/10.1016/j.tecto.2005.11.021>
- Thybo, H., Bulut, N., Grund, M., Mauerberger, A., Makushkina, A., Artemieva, I. M., et al. (2021). ScanArray-A broadband seismological experiment in the Baltic shield. *Seismological Research Letters*, 92(5), 2811–2823. <https://doi.org/10.1785/0220210015>
- Treitel, S., & Robinson, E. (1966). Seismic wave propagation in layered media in terms of communication theory. *Geophysics*, 31(1), 17–32. <https://doi.org/10.1190/1.1439729>
- Ulrych, T. J., Somerville, P. G., Jensen, O. G., & Ellis, R. M. (1972). Homomorphic deconvolution of some Teleseismic events. *Bulletin of the Seismological Society of America*, 62(5), 1269–1281. <https://doi.org/10.1785/BSSA0620051269>
- Vallée, M., Charléty, J., Ferreira, A. M. G., Delouis, B., & Vergoz, J. (2011). SCARDEC: A new technique for the rapid determination of seismic moment magnitude, focal mechanism and source time functions for large earthquakes using body-wave deconvolution. *Geophysical Journal International*, 184(1), 338–358. <https://doi.org/10.1111/j.1365-246X.2010.04836.x>
- Vinnik, L. P., Chenet, H., Gagnepain-Beyneix, J., & Lognonne, P. (2001). First seismic receiver functions on the Moon. *Geophysical Research Letters*, 28(15), 3031–3034. <https://doi.org/10.1029/2001gl012859>
- Vinnik, L. P., Reigber, C., Aleshin, I. M., Kosarev, G. L., Kaban, M. K., Oreshin, S. I., & Roecker, S. W. (2004). Receiver function tomography of the central Tien Shan. *Earth and Planetary Science Letters*, 225(1–2), 131–146. <https://doi.org/10.1016/j.epsl.2004.05.039>
- Wang, J., Wang, Q., Xu, C. B., Dan, W., Xiao, Z., Shu, C. T., & Wei, G. (2022). Cenozoic delamination of the southwestern Yangtze craton owing to densification during subduction and collision. *Geology*, 50(8), 912–917. <https://doi.org/10.1130/G49732.1>
- Wang, R. J. (1999). A simple orthonormalization method for stable and efficient computation of Green's functions. *Bulletin of the Seismological Society of America*, 89(3), 733–741. <https://doi.org/10.1785/BSSA0890030733>
- Wang, W., Wu, J., & Hammond, J. O. S. (2021). Mantle dynamics beneath the Sichuan basin and eastern Tibet from Teleseismic tomography. *Tectonics*, 40(2). <https://doi.org/10.1029/2020TC006319>
- Wang, X., Chen, L., Ai, Y. S., Xu, T., Jiang, M. M., Ling, Y., & Gao, Y. (2018). Crustal structure and deformation beneath eastern and northeastern Tibet revealed by P-wave receiver functions. *Earth and Planetary Science Letters*, 497, 69–79. <https://doi.org/10.1016/j.epsl.2018.06.007>

- Wei, Y., Zhang, S., Li, M., Wu, T., Hua, Y., Zhang, Y., & Cai, J. (2022). Regional lithospheric deformation beneath the East Qinling-Dabie orogenic belt based on ambient noise tomography. *Geophysical Journal International*, 228(2), 1294–1312. <https://doi.org/10.1093/gji/ggab393>
- Wessel, P., Luis, J. F., Uieda, L., Scharroo, R., Wobbe, F., Smith, W. H. F., & Tian, D. (2019). The generic mapping tools version 6. *Geochemistry, Geophysics, Geosystems*, 20(11), 5556–5564. <https://doi.org/10.1029/2019gc008515>
- Wessel, P., & Smith, W. H. F. (1995). New version of the generic mapping tools. *Eos. Transactions - American Geophysical Union*, 76(33), 329. <https://doi.org/10.1029/95EO00198>
- Wilson, D. C., Angus, D. A., Ni, J. F., & Grand, S. P. (2006). Constraints on the interpretation of S-to-P receiver functions. *Geophysical Journal International*, 165(3), 969–980. <https://doi.org/10.1111/j.1365-246X.2006.02981.x>
- Wu, Q., Tian, X., Zhang, N., Li, W., & Zeng, R. (2003a). Receiver function estimated by maximum entropy deconvolution. *Acta Seismologica Sinica*, 25(4), 382–389. <https://doi.org/10.1007/s11589-003-0073-y>
- Wu, Q., Tian, X., Zhang, N., Li, W., & Zeng, R. (2003b). Receiver function estimated by wiener filtering. *Earthquake Research in China*, 19(1), 41–47.
- Xia, X., Li, Z., Bao, F., Xie, J., Shi, Y., You, Q., & Chen, H. (2021). Sedimentary structure of the Sichuan Basin derived from seismic ambient noise tomography. *Geophysical Journal International*, 225(1), 54–67. <https://doi.org/10.1093/gji/ggaa578>
- Xu, Q., Pei, S., Yuan, X., Zhao, J., Liu, H., Tu, H., & Chen, S. (2019). Seismic evidence for lateral Asthenospheric flow beneath the northeastern Tibetan Plateau derived from S receiver functions. *Geochemistry, Geophysics, Geosystems*, 20(2), 883–894. <https://doi.org/10.1029/2018GC007986>
- Xu, Q., Zhao, J., Yuan, X., Liu, H., & Pei, S. (2017). Detailed configuration of the underthrusting Indian lithosphere beneath Western Tibet revealed by receiver function images. *Journal of Geophysical Research-Solid Earth*, 122(10), 8257–8269. <https://doi.org/10.1002/2017JB014490>
- Xu, T., Wu, Z., Zhang, Z., Tian, X., Deng, Y., Wu, C., & Teng, J. (2014). Crustal structure across the Kunlun fault from passive source seismic profiling in East Tibet. *Tectonophysics*, 627, 98–107. <https://doi.org/10.1016/j.tecto.2013.11.010>
- Xu, X., Ding, Z., Shi, D., & Li, X. (2013). Receiver function analysis of crustal structure beneath the eastern Tibetan plateau. *Journal of Asian Earth Sciences*, 73, 121–127. <https://doi.org/10.1016/j.jseaes.2013.04.018>
- Xu, Y., He, B., Huang, X., Luo, Z., Chung, S., Xiao, L., et al. (2007). Identification of mantle plumes in the emeishan large igneous province. *Episodes*, 30(1), 32–42. <https://doi.org/10.18814/epiugs/2007/v30i1/005>
- Yang, H., Peng, H., & Hu, J. (2017). The lithospheric structure beneath southeast Tibet revealed by P and S receiver functions. *Journal of Asian Earth Sciences*, 138, 62–71. <https://doi.org/10.1016/j.jseaes.2017.02.001>
- Yao, H. (2020). Building the community velocity model in the Sichuan-Yunnan region, China: Strategies and progresses. *Science China Earth Sciences*, 63(9), 1425–1428. <https://doi.org/10.1007/s11430-020-9645-3>
- Yao, H., Beghein, C., & van der Hilst, R. D. (2008). Surface wave array tomography in SE Tibet from ambient seismic noise and two-station analysis - II. Crustal and upper-mantle structure. *Geophysical Journal International*, 173(1), 205–219. <https://doi.org/10.1111/j.1365-246X.2007.03696.x>
- Yuan, H., & Romanowicz, B. (2010). Lithospheric layering in the North American craton. *Nature*, 466(7310), 1063–1068. <https://doi.org/10.1038/nature09332>
- Yuan, X., Kind, R., Li, X., & Wang, R. (2006). The S receiver functions: Synthetics and data example. *Geophysical Journal International*, 165(2), 555–564. <https://doi.org/10.1111/j.1365-246X.2006.02885.x>
- Zhang, G., He, Y., Ai, Y., Jiang, M., Mon, C. T., Hou, G., et al. (2021). Indian continental lithosphere and related volcanism beneath Myanmar: Constraints from local earthquake tomography. *Earth and Planetary Science Letters*, 567, 116987. <https://doi.org/10.1016/j.epsl.2021.116987>
- Zhang, H., Teng, J., Tian, X., Zhang, Z., Gao, R., & Liu, J. (2012). Lithospheric thickness and upper-mantle deformation beneath the NE Tibetan Plateau inferred from S receiver functions and SKS splitting measurements. *Geophysical Journal International*, 191(3), 1285–1294. <https://doi.org/10.1111/j.1365-246X.2012.05667.x>
- Zhang, L., Hu, Y. L., Qin, M., Duan, Y., Duan, Y. Z., Peng, H. C., et al. (2015). Study on crustal and lithosphere thicknesses of Tengchong volcanic area in Yunnan. *Chinese Journal of Geophysics*, 58(5), 1622–1633. <https://doi.org/10.6038/cjg20150514>
- Zhang, R., Wu, Q., Sun, L., He, J., & Gao, Z. (2014). Crustal and lithospheric structure of Northeast China from S-wave receiver functions. *Earth and Planetary Science Letters*, 401, 196–205. <https://doi.org/10.1016/j.epsl.2014.06.017>
- Zhang, Y., Chen, L., Ai, Y., & Jiang, M. (2019). Lithospheric structure beneath the central and Western North China Craton and adjacent regions from S-receiver function imaging. *Geophysical Journal International*, 219(1), 619–632. <https://doi.org/10.1093/gji/ggz322>
- Zhang, Y., Chen, L., Ai, Y., Jiang, M., Xu, W., & Shen, Z. (2018). Lithospheric structure of the south China block from S-receiver function. *Chinese Journal of Geophysics-Chinese Edition*, 61(1), 138–149. <https://doi.org/10.6038/cjg2018L0226>
- Zhang, Z., Yuan, X., Chen, Y., Tian, X., Kind, R., Li, X., & Teng, J. (2010). Seismic signature of the collision between the east Tibetan escape flow and the Sichuan Basin. *Earth and Planetary Science Letters*, 292(3–4), 254–264. <https://doi.org/10.1016/j.epsl.2010.01.046>
- Zheng, X., Yao, Z.-X., Liang, J.-H., & Zheng, J. (2010). The role played and opportunities provided by IGP DMC of China national seismic network in wenchuan earthquake disaster relief and researches. *Bulletin of the Seismological Society of America*, 100(5B), 2866–2872. <https://doi.org/10.1785/0120090257>
- Zhou, L., Xie, J., Shen, W., Zheng, Y., Yang, Y., Shi, H., & Ritzwoller, M. H. (2012). The structure of the crust and uppermost mantle beneath South China from ambient noise and earthquake tomography. *Geophysical Journal International*, 189(3), 1565–1583. <https://doi.org/10.1111/j.1365-246X.2012.05423.x>

References From the Supporting Information

- Heit, B., Sodoudi, F., Yuan, X., Bianchi, M., & Kind, R. (2007). An S receiver function analysis of the lithospheric structure in South America. *Geophysical Research Letters*, 34(14), L14307. <https://doi.org/10.1029/2007gl030317>
- Huang, M.-H., Buergermann, R., & Freed, A. M. (2014). Probing the lithospheric rheology across the eastern margin of the Tibetan Plateau. *Earth and Planetary Science Letters*, 396, 88–96. <https://doi.org/10.1016/j.epsl.2014.04.003>
- Liu, Z., Tian, X., Yuan, X., Liang, X., Chen, Y., Zhu, G., et al. (2020). Complex structure of upper mantle beneath the Yadong-Gulu rift in Tibet revealed by S-to-P converted waves. *Earth and Planetary Science Letters*, 531, 115954. <https://doi.org/10.1016/j.epsl.2019.115954>
- Meng, F. C., Ai, Y. S., Xu, T., Chen, L., Wang, X., & Li, L. (2021). Lithospheric structure beneath the boundary region of north China craton and Xing Meng orogenic belt from S-receiver function analysis. *Tectonophysics*, 818, 229067. <https://doi.org/10.1016/j.tecto.2021.229067>

- Wu, Z., Chen, L., Talebian, M., Wang, X., Jiang, M., Ai, Y., et al. (2021). Lateral structural variation of the lithosphere-asthenosphere system in the northeastern to eastern Iranian plateau and its tectonic implications. *Journal of Geophysical Research-Solid Earth*, 126(1). <https://doi.org/10.1029/2020jb020256>
- Xu, S., Unsworth, M. J., Hu, X., & Mooney, W. D. (2019). Magnetotelluric evidence for asymmetric simple shear extension and lithospheric thinning in south China. *Journal of Geophysical Research-Solid Earth*, 124(1), 104–124. <https://doi.org/10.1029/2018jb016505>
- Zhao, W., Kumar, P., Mechie, J., Kind, R., Meissner, R., Wu, Z., et al. (2011). Tibetan plate overriding the Asian plate in central and northern Tibet. *Nature Geoscience*, 4(12), 870–873. <https://doi.org/10.1038/ngeo1309>